Materials Advances

ROYAL SOCIETY OF CHEMISTRY

PAPER

View Article Online
View Journal | View Issue

Check for updates

Cite this: *Mater. Adv.*, 2024, **5**, 7278

Pioneering the design of S-scheme SnS_2/g-C_3N_4 nanocomposites *via* sonochemical and physical mixing methods for solar degradation of cationic rhodamine B dye

Ali Alsalme,[a] Mustafa Hesham,[b] Ayman Soltan,[c] Nagy N. Mohammed,[b] A. Qassim Nejm,[b] M. F. Abdel Messih,[b] Islam A. Hussein[b] and M. A. Ahmed *[b]

Since the advent of photocatalysis, various research studies have been devoted to exploring novel high-performance photocatalysts for converting solar energy into chemical energy. However, the employment of natural solar radiation in the degradation of organic pollutants has not been attained until now. This novel research work recorded the employment of natural solar illumination in degrading rhodamine B [RhB] dye on the surface of S-scheme SnS_2/g-C_3N_4 heterojunctions. SnS_2/g-C_3N_4 heterojunctions containing different rational compositions of g-C_3N_4 and SnS_2 nanoparticles were synthesized *via* sonochemical and physical mixing approaches. Sonochemistry is a novel approach with multiple applications and is of significant importance since ultrasonic waves form acoustic cavitation in solutions, enhancing chemical activity with remarkable economic value. The textural, optical and nanostructural properties of the heterojunctions were investigated through diffuse reflectance spectroscopy [DRS], high-resolution transmission electron microscopy [HRTEM], photoluminescence [PL], N_2-adsorption–desorption isotherms, scanning electron microscopy [SEM], energy dispersive X-ray spectroscopy [EDX], X-ray diffraction [XRD], electrochemical impedance spectroscopy [EIS] and X-ray photoelectron spectroscopy [XPS]. The diffraction results from XRD, HRTEM and SAED analyses revealed remarkable distortion in the crystalline properties of g-C_3N_4 upon the introduction of SnS_2 nanoparticles, implying a strong chemical interaction between SnS_2 nanoparticles and g-C_3N_4 sheets, which manifested the construction of an effective heterojunction. Homogeneous deposition of SnS_2 nanoparticles on g-C_3N_4 sheets was achieved through a sonochemical route. However, SnS_2 nanoparticle agglomeration was recorded on g-C_3N_4 sheets synthesized by means of a physical mixing process. Photocatalytic experimental results revealed the degradation of 34% of RhB dye on g-C_3N_4 sheets due to the limited absorption of natural solar radiation and the fast and uncontrolled electrostatic forces between electron–hole pairs. By incorporating 5, 10, 15 and 20 wt% SnS_2 nanoparticles in the ultrasonic bath on g-C_3N_4 sheets, the amount of RhB dye discharge was raised to 51, 78, 98 and 69%, respectively, during two hours of sunlight illumination. Alternatively, only 55% of RhB dye was decomposed on the surface of CNSnS15 synthesized through the physical mixing route. Hydroxyl radicals played a crucial role in the degradation of RhB dye, as proved by the PL of terephthalic acid and scavenger trapping experiments. The charge transport mechanism followed the S-scheme mechanism, as elucidated from scavenger trapping experiments. The novel as-synthesized sonicated SnS_2/g-C_3N_4 nanocomposite is considered a promising photocatalyst in degrading organic pollutants under low-cost natural solar radiation.

Received 15th July 2024,
Accepted 6th August 2024

DOI: 10.1039/d4ma00718b

rsc.li/materials-advances

1. Introduction

The discharge of toxic organic dyes from textile and food industries pollute water resources, posing serious threats to human health and aquatic life.[1–5] The complex chemical nature of antibiotics, dyes and pesticides resists their decomposition *via* traditional routes.[5–10] Electrochemical methods, coagulation, reverse osmosis, ion exchange and adsorption have failed

---

[a] *Department of Chemistry, College of Science, King Saud University, P.O. 2455, Riyadh 11451, Saudi Arabia*
[b] *Chemistry Department, Faculty of Science, Ain Shams University, Egypt. E-mail: abdelhay71@hotmail.com*
[c] *Department of Chemistry, University of York, York YO10 5DD, UK*

to mitigate these toxic organic pollutants. Photocatalysis green technology has been used to degrade organic pollutants into eco-friendly species on the surface of semiconductors under solar energy.[11–15] MnO_2, ZnS, TiO_2, $Bi_2O_2CO_3$, MoO_3, CeO_2 and ZnO recorded strong photocatalytic reactivity in the fragmentation of organic pollutants under UV radiation.[16–20] However, the ultrafast Coulombic attraction force between electron–hole pairs and the poor absorbability of solar radiation reduces the efficiency of the photocatalytic process. Recently, more focus has been paid to metal-free g-C_3N_4 sheets as a low-cost, valuable photocatalyst for solving water and energy crises. The strong chemical stability due to the conjugated system, biocompatibility, low toxicity and cost-effectiveness of g-C_3N_4 has attracted the attention of various researchers in recent years.[21–28] Various investigations have been devoted to verify the photocatalytic reactivity of g-C_3N_4 in the degradation of different organic wastes.[11] The experimental results revealed that g-C_3N_4 cannot meet the practical applications in breaking down the organic pollutants due to the low tendency to capture solar radiation, low quantum efficiency, fast Coulombic recombination rate and poor oxidative efficiency of the positive holes. Several tactics were devoted to overcoming the shortcomings of g-C_3N_4, such as coupling with strong oxidative semiconductors to enhance the oxidative power of the heterojunction and concentrating on the production of photoinduced charge carriers. SnS_2 nanoparticles with narrow band gap energy, good thermal stability, non-toxicity and broad spectral response are considered novel visible light-driven photocatalysts.[29–32] Thi *et al.* synthesized SnS_2/g-C_3N_4 by direct calcination method for photocatalytic mitigation of rhodamine B dye.[33] During the synthesis, g-C_3N_4 played a buffer role in exfoliating SnS_2, whereas SnS_2 accelerated the destruction of g-C_3N_4 at high temperatures, resulting in an N-deficiency form with enhanced charge transport. The experimental results implied that SnS_2 enhanced the absorbability and the photocatalytic performance.[33] Liu *et al.* synthesized SnS_2/g-C_3N_4 by ion exchange for the successful photocatalytic degradation of methyl orange dye.[34] The corresponding photocatalytic power was attributed to the role of SnS_2 in limiting the electron–hole recombination of g-C_3N_4 sheets. Hydrothermal synthesis of SnS_2/g-C_3N_4 was carried out by Gao *et al.* for expelling methyl orange dye under visible light. The results implied the degradation of 93% of methyl orange dye (MO), which referred to Z-scheme nanocomposite production with appropriate charge carrier separation and transportation.[35] The experimental results implied that SnS_2 increased the concentration of the charge carriers by controlling the electron–hole recombination rate. Shyagathur *et al.* recorded that only 55% of methylene blue dye was degraded on SnS_2/g-C_3N_4, prepared using the hydrothermal method, due to the weak charge transport and separation of the charge carriers.[36] Shyagathur *et al.* noticed that mixing RGO with SnS_2/g-C_3N_4 was the main requirement for enhancing the degradation of methylene blue due to the role of RGO in enhancing the charge diffusion between SnS_2 and g-C_3N_4 semiconductors.[36] Cheng *et al.* synthesized SnS_2/g-C_3N_4 by solvothermal method to degrade rhodamine B dye besides photocatalytic hydrogen production.[37] The experimental results implied the strong efficiency of the as-synthesized samples in the photocatalytic process, which is attributed to the enhanced transport and separation of the photogenerated electron–hole pairs. Song *et al.* synthesized g-C_3N_4/SnS_2 van der Waals heterojunctions by embedding SnS_2 crystals in thin g-C_3N_4 nanosheets to enhance the hydrogen evolution and the degradation of organic pollutants. The photocatalytic performance was evaluated, showing that the g-C_3N_4/SnS_2 heterojunctions demonstrated outstanding 2,4-dichlorophenol (2,4-DCP) photo-oxidation and Cr(VI) photoreduction capabilities simultaneously. Under visible light irradiation for 2 hours, 85% of Cr(VI) and 94% of 2,4-DCP were eliminated in the mixed solution. Furthermore, the hydrogen evolution rate increased to approximately 6.58 times that of g-C_3N_4.[38] Zhu *et al.* successfully synthesized ultrafine SnS_2 supported on a porous g-C_3N_4 sheet (SnS_2/g-C_3N_4) 0D/2D heterojunction adopting a solvothermal process to degrade rhodamine B (RhB) under visible light. The photodegradation efficiency reached 96.8% after 105 minutes of irradiation, with a reaction rate constant (k) of 3.3% min^{-1}, showing 8.25 and 8.05 times enhancement compared to pure g-C_3N_4 and SnS_2, respectively. Furthermore, trapping experiments confirmed that the superoxide radicals and holes (h^+) are the primary active species in this photocatalytic system.[39] Tamilarasu *et al.* developed MoS_2–SnS_2@g-C_3N_4 catalysis *via* the conventional hydrothermal method. The degradation efficiency of the synthesized samples was assessed using methylene blue dye. The photodegradation efficiency reached 86.6% after 90 minutes of irradiation.[40] Alnahdi *et al.* prepared 3DF-SnS_2/g-C_3N_4 photocatalysts using a simple solvothermal method. The photocatalytic performance was evaluated by following the decomposition of rhodamine B [RhB] dye. Compared to other nanohybrids in the study, the optimized 3DF-SnS_2/g-C_3N_4 structure showed excellent efficiency in degrading 90.15% RhB dye.[41] Thanh *et al.* successfully fabricated SnS_2/g-C_3N_4 composites with SnS_2 nanosheets on a porous g-C_3N_4 substrate. The composites exhibited superior rhodamine B [RhB] photodegradation compared to pure SnS_2 and g-C_3N_4, achieving a maximum removal efficiency of 92.22% after 6 hours of light irradiation.[42] Fan *et al.* successfully synthesized g-C_3N_4/Ag_2S/SnS_2 with Ag_2S quantum dots as electron mediators through the ion exchange process and self-peeling of sheets of g-C_3N_4. Compared with the pristine materials, the photocatalyst g-C_3N_4/Ag_2S/SnS_2 demonstrated significantly enhanced photocatalytic performance under visible light exposure.[43] Liu *et al.* synthesized g-C_3N_4/SnS_2 nanocomposites to eliminate hexavalent uranium (U(VI)). Two-dimensional (2D) hexagonal SnS_2 nanosheets were incorporated to enhance the absorbability of the nanocomposites. Notably, during the photocatalytic test under sunlight, the U(VI) removal rate using 0.08-SnCN reached 90% within 2 hours. The findings of the experimental results suggested that U(VI) was reduced by superoxide radicals.[44] All the previous research studies were concentrated on the synthesis of SnS_2/g-C_3N_4 nanocomposite through hydrothermal, solvothermal, ion exchange and co-precipitation routes that consumed huge amounts of energy and accompanied by poor distribution of SnS_2 on g-C_3N_4 sheets.[33–38] A drawback of the traditional synthesis method is the long duration of synthesis, which is due to the time taken to attain homogeneity in temperature using autoclaves and conventional heating systems. Therefore, there is a great need to fabricate novel photocatalysts by applying ultrasonic waves generated in the ultrasonic bath to act as an energy supplier for depositing nanoparticles on g-C_3N_4 sheets. The sonochemical process is a clean and efficient synthesis route that prohibits the reaction with a huge amount of energy for accelerating the reactant molecules to hybridize with each other and produce effective heterojunctions. Sonochemistry is responsible for the production of hotspots that generate extraordinary materials with manipulated morphologies and structures. Ultrasound is a longitudinal wave type with a high frequency of 20 kHz, surpassing the upper human auditory perception limit.[45] Air cavities, shock waves and air bubbles are produced in the sonochemical bath to prevent the transfer of excessive energy to the reaction medium. The reaction occurs inside the bubble among the chemical precursors. The emerged bubbles undergo rapid and excessive expansion, causing their size to increase dramatically compared to the equilibrium radius, followed by eventual collapse. Upon collapse, the stored concentrated energy within the bubble is rapidly released in a short time, resulting in around 5000 K extremely localized and transient temperatures and nearly 1000 bar pressures, according to the thermal ''hot spot'' theory.[45] These features usually generate the heterojunction by homogeneous dispersion of the guest materials on the sheets of g-C_3N_4. Compared with conventional methods, ultrasound-assisted methods are valuable in accelerating chemical reactions, generating a new phase and influencing the structure and surface of the synthesized particles

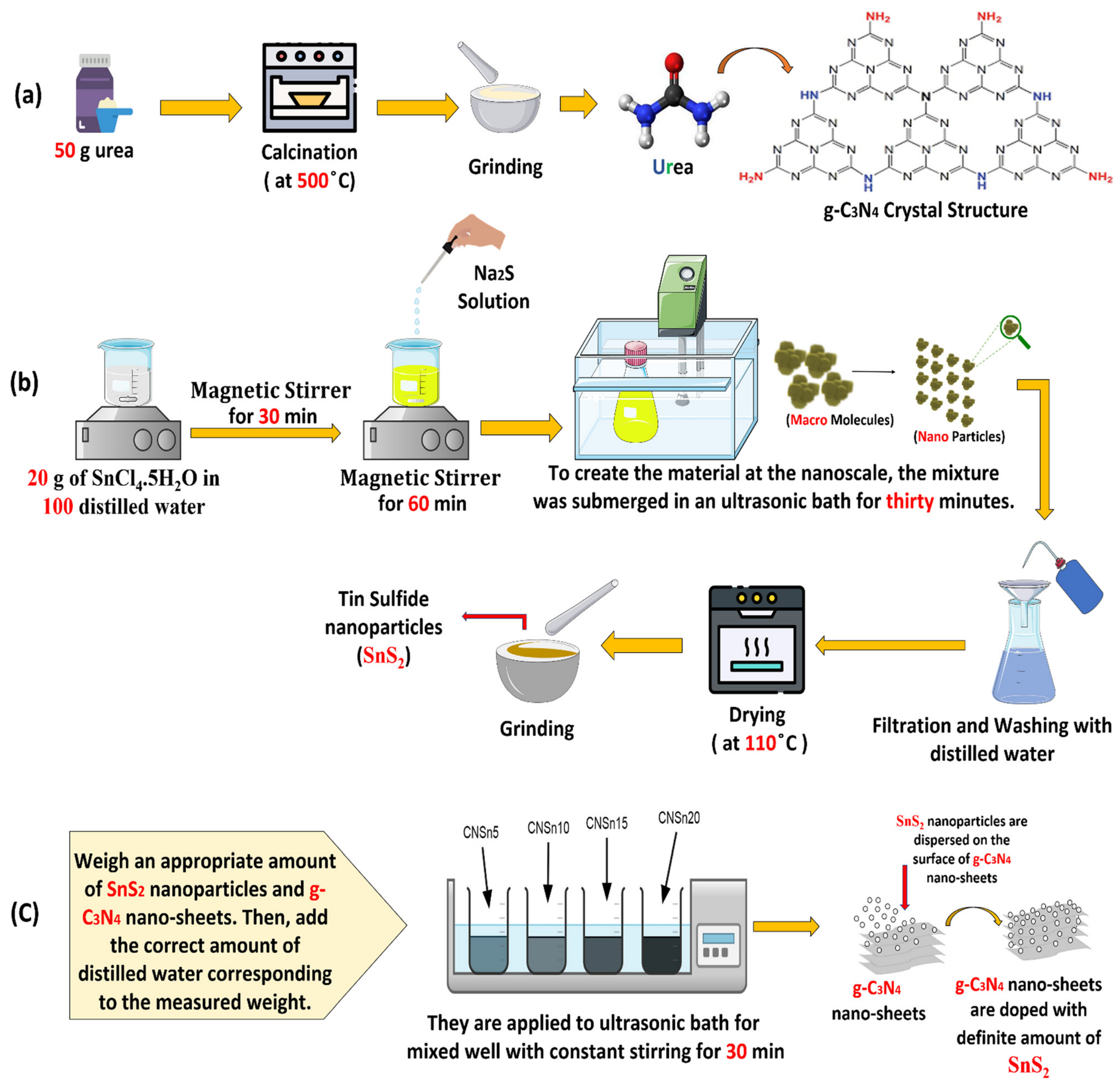

Fig. 1 Scheme for the synthesis of (a) g-C_3N_4, (b) SnS_2 and (c) SnS_2/g-C_3N_4 nanocomposites.

through acoustic cavitation. Moreover, the photocatalytic performance of SnS_2/g-C_3N_4 nanocomposites in expelling organic dyes was investigated by previous researchers under UV and visible light radiations, which constitute only 50% of the natural sunlight radiation. However, the employment of natural solar radiation with strong power [600–1200] W to expel various organic pollutants on SnS_2/g-C_3N_4 nanocomposite containing various proportions of photothermal SnS_2 photocatalyst has not been studied until now. In this novel research, a successful manipulation of S-scheme SnS_2/g-C_3N_4 heterojunctions embedded in various concentrations of SnS_2 and g-C_3N_4 was carried out. The surface investigation and the morphological changes are investigated by EDX, XRD, XPS, SEM, Mapping, DRS, HRTEM, PL and N_2-adsorption–desorption developed techniques. The photocatalytic power of hybrid SnS_2/g-C_3N_4 heterojunctions was detected by following the fragmentation of RhB dye under natural solar radiation of 1000 W power. The experimental results for photocatalytic degradation of rhodamine B dye on the optimum sample CNSnS15 heterojunction synthesized by the sonochemical and physical mixing processes were compared to give a clear clue on the effect of preparation mode on the efficiency of the photocatalyst. S-scheme charge diffusion was suggested to record the electron–hole transfer mechanism based on the results of trapping experiments and terephthalic PL analysis. The novel SnS_2/g-C_3N_4 heterojunction could be considered a successful photocatalyst for utilizing natural solar radiation in the degradation of various organic pollutants dispersed in wastewater.

2. Experimental research work

2.1. Material

The reagents and solvents utilized in this study are all of analytical grade, and they were all used exactly as supplied. We obtained pure ammonia solution (NH_4OH) (M_{wt} = 17.031 g mol^{-1}, ≥25%), ammonium oxalate ($(NH_4)_2C_2O_4$) (M_{wt} = 124.01 g mol^{-1}, ≥99%), urea (M_{wt} = 60.06 g mol^{-1}, ≥99%), sodium sulfide (Na_2S), benzoquinone ($C_6H_4O_2$) (M_{wt} = 108.09 g mol^{-1}, ≥99%), tin(IV) chloride ($SnCl_4{\cdot}5H_2O$), terephthalic acid ($C_6H_4(CO_2H)_2$) (M_{wt} = 166.13 g mol^{-1}, ≥99%), and isopropanol (C_3H_8O) (M_{wt} = 60.096 g mol^{-1}, ≥99%) from Fluka Company.

2.2. Preparation of pristine materials and heterojunctions

2.2.1 Preparation of g-C_3N_4 sheets. Microcrystalline highly purified urea (100 g) was exposed to heating in a porcelain reactor under air flow from room temperature to 540 °C by fixed and low rate process [Fig. 1a]. The reactor was calcined at 540 °C for five hours for complete condensation of urea and evolution of ammonia gas. The reactor was left under ambient conditions for 24 hours in the closed muffle for slow cooling. Spongy g-C_3N_4 sheets were generated with muff color in the porcelain mortar. Finally, a mild grinding of the resultant solid specimen was carefully carried out to prevent the deterioration of the sample.

2.2.2. Preparation of SnS_2 semiconductor. $SnCl_4{\cdot}5H_2O$ (27 g) was dissolved in freshly prepared bi-distilled water with constant stirring for 50 minutes. A solution of sodium sulfide dissolved in bi-distilled water was added to the stannic chloride solution drop by drop till the formation of a black precipitate of SnS_2 [Fig. 1b]. The black precipitate was irradiated sonochemically for 40 minutes in a 200 W ultrasonic bath. Then, the sonicated SnS_2 was collected by filtration, followed by washing with bi-distilled water to remove any foreign materials. Finally, the solid specimen was dried at 115 °C for eight hours.

2.2.3. Preparation of SnS_2/g-C_3N_4 by sonochemical route. A stoichiometric amount of pristine SnS_2 and g-C_3N_4 sheets distributed in bi-distilled water were coupled in an ultrasonic bath of 200 W power for 50 min for obtaining 5, 10 and 15 wt% of SnS_2/g-C_3N_4 [Fig. 1c]. Then, each of the sonicated mixtures was filtered and purified extensively with distilled water. The above mixtures were dried at 110 °C for 24 hours. The photocatalysts were denoted as g-C_3N_4, SnS_2, CNSn5, CNSn10, CNSn15 and CNSn20 for pristine g-C_3N_4, SnS_2 and the solid samples embedded 5, 10, 15 and 20 wt% SnS_2, respectively.

2.2.4. Preparation of SnS_2/g-C_3N_4 by physical mixing method. SnS_2 nanoparticles (0.15 g) and 0.85 g of g-C_3N_4 were mixed together in porcelain mortar and ground. After a while, the mixture is subjected to a vortex shaker for 30 min to ensure the homogeneity of the as-synthesized heterojunction. Finally, the solid specimens were subjected to drying at 100 °C overnight to obtain 15 wt% SnS_2 deposited on g-C_3N_4 by the physical mixing process.

2.3. Characterization techniques

PAnalytical X'PERT MPD diffractometer analyzed the remarked features of the as-synthesized pristine materials and the nanocomposites with 2θ values varied from 10–70°. The experimental adsorption isotherms were evaluated to investigate the textural properties and detect the surface area. The particle configuration was evaluated with HRTEM [JOEL]. The electronic structure and the elemental composition were verified by

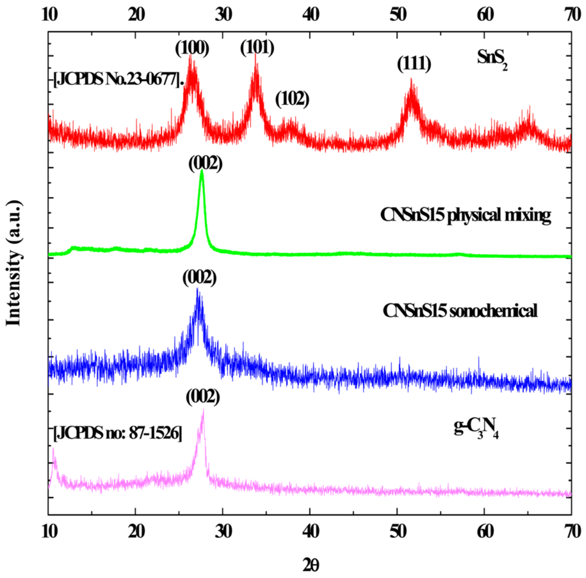

Fig. 2 XRD of g-C_3N_4, SnS_2 and CNSnS15 prepared *via* the sonochemical method and CNSnS15 prepared *via* physical mixing.

Thermo Fisher Scientific XPS. DRS curves were constructed by a JASCO spectrometer (V-570) for band energy structure estimation. The photoluminescence of the solid sample was estimated using a Thermo Fischer technique for predicting the charge carrier separation efficiency. The photocatalytic degradation of RhB dye under natural sunlight radiation was carried out to record the heterojunction photocatalytic performance for the nanocomposite-embedded definite compositions of SnS_2. The extent of adsorption of the solid samples was determined under dark conditions by directing 100 ml of 2×10^{-5} M RhB dye to 0.05 g of the photocatalyst under dark conditions for 60 minutes. Then, the mixture of the solid–dye solution was irradiated with natural solar radiation of 1000 W power for 120 minutes. Stoichiometric proportions of the dye–photocatalyst mixture were taken off at definite interval times to analyze the remainder concentration of the RhB dye solution using spectrophotometer progress. Isopropanol, benzoquinone and ammonium oxalate are three types of scavengers of concentration 1×10^{-3} M, which were added separately to the mixture of dye solution and photocatalyst under the same reaction parameters to monitor the nature of reactive species responsible for the redox reaction. PL spectrum of alkaline terephthalic acid solution was recorded to identify the nature and concentration of the hydroxyl radicals.

3. The experimental results

3.1. Physical properties

The crystalline properties of the pristine $g\text{-}C_3N_4$, SnS_2 and CNSnS15 heterojunction prepared by sonochemical and

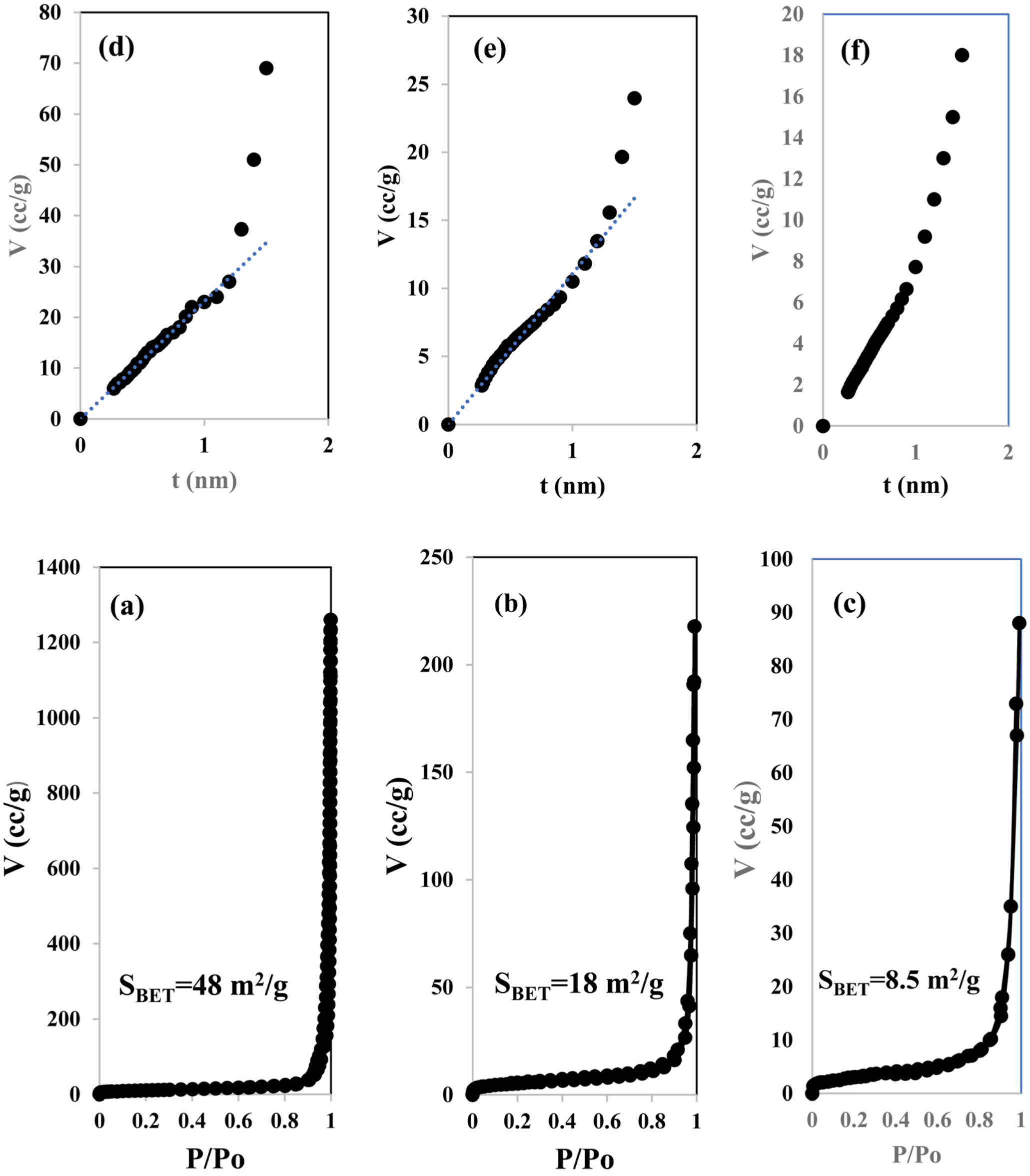

Fig. 3 N_2-adsorption isotherms of (a) $g\text{-}C_3N_4$ and (b) CNSnS15 synthesized *via* the sonochemical route and (c) CNSnS15 synthesized *via* physical mixing. V_a–t plot for (d) $g\text{-}C_3N_4$ and (e) CNSnS15 synthesized *via* the sonochemical route and (f) CNSnS15 synthesized *via* physical mixing.

physical mixing methods were determined by XRD [Fig. 2]. XRD pattern of g-C_3N_4 showed diffraction peaks at 2θ = 27.18 and 13.08, which ascribed to (002) and (100) planes of orthorhombic phase [JCPDS no: 87-1526]. On the other hand, the XRD pattern of SnS_2 showed diffraction peaks at 2θ =28.2, 32.4 and 52° referred to (100), (101) and (102) planes of the hexagonal structure with the $P\bar{3}m1$ space group [JCPDS No. 23-0677]. XRD pattern of CNSnS15 prepared by sonochemical and physical mixing methods showed the main diffraction pattern of the (002) plane of g-C_3N_4 sheets and (011) plane of SnS_2, implying the successful heterojunction generation. The peak intensity of the (002) plane of orthorhombic g-C_3N_4 reduced with deposition of 15 wt% of SnS_2 on the g-C_3N_4 surface. However, the (001) plane of orthorhombic g-C_3N_4 completely disappeared. The remarkable shift in the diffraction peak positions of g-C_3N_4 to a low diffraction angle was recorded, revealing the damage in the crystalline structure of g-C_3N_4 sheets by introducing SnS_2 nanoparticles as a result of the simultaneous coupling between SnS_2 nanoparticles and g-C_3N_4 sheets for constructing an effective SnS_2/g-C_3N_4 heterojunction [Fig. 2]. The crystalline size estimated by the Debye Scherrer equation from the most intense peak is 27, 9.1, 11.4 and 22.8 for g-C_3N_4, SnS_2, and CNSnS15 prepared by sonochemical and physical mixing processes, respectively. The peak intensity of g-C_3N_4 sheets and SnS_2 are strongly decremented in the heterojunction with the incorporation of 15 wt% SnS_2, which was ascribed to coupling g-C_3N_4 and SnS_2 under the sonochemical condition. It is well known that the waves, air bubbles, shocks and air cavities generated in the ultrasonic bath with high frequency break down large agglomerates into particles in nanodimensions. Recent experimental studies revealed that the incorporation of SnS_2 on g-C_3N_4 shifted the peak position to a small angle, implying the strong chemical interaction between SnS_2 and g-C_3N_4 sheets[32–34]

Fig. 3 illustrates the physisorption isotherms of nitrogen gas at 77 K on pristine g-C_3N_4 and CNSnS15 heterojunction synthesized by sonochemical and physical mixing processes. The adsorption isotherms of the as-synthesized samples are classified as type II isotherms, which refer to the non-porous solid structure [Fig. 3a–c]. The surface area of g-C_3N_4 and CNSnS15 prepared by sonochemical and physical mixing methods evaluated from the BET equation was 48, 18 and 8.4 $m^2\ g^{-1}$, respectively. The surface area measurements revealed a depression in 60% g-C_3N_4 surface area of the solid sample prepared by the sonochemical route, which implied that the strong adhesion of SnS_2 nanoparticles on g-C_3N_4 sheets decremented the surface area available to adsorb N_2 gas that was further proved by HRTEM analysis. However, a drastic depression in the surface area of g-C_3N_4 by 80% for the sample prepared by the physical mixing method revealed the agglomeration of SnS_2 nanoparticles on g-C_3N_4 sheets. Although the adsorption–desorption isotherm is completely reversible, the corresponding V_a–t plot indicated that the solid specimens are porous where an upward deviation is taking place in the three cases [Fig. 3d–f]. The absence of a hysteresis loop from these isotherms showed that no capillary condensation was taking place, a characteristic related to macro-or non-porous solids; however, the upward deviation in the V_a–t plots indicated the presence of pores that fall in the mesoporous range. This phenomenon is interpreted as reversible capillary condensation controlled by the size (wide micro and narrow mesopores) and the shape (cones and wedges) of the pores. This reversible capillary condensation in the N_2 adsorption process followed the same mechanism on desorption, making the adsorption isotherm free of any hysteresis. SEM defined the morphology of the heterojunction, which clarifies the dispersion of SnS_2 nanoparticles with large amounts on the surface of g-C_3N_4 sheets [Fig. 4a]. These results reflected the strong chemical affinity of SnS_2 nanoparticles to adhere strongly on g-C_3N_4 sheets. Mapping and EDX analysis were carried out to analyze the compositions of the sonicated CNSnS15 heterojunction and to verify the dispersion of SnS_2 and g-C_3N_4 with respect to each other. The experimental results extracted from mapping and EDX analysis revealed that C, N, Sn and S are the main constituents of the SnS_2/g-C_3N_4 heterojunction without any other impurities [Fig. 4b–g]. Mapping analysis revealed the homogeneous chemical dispersion of SnS_2 on g-C_3N_4 sheets. HRTEM analysis investigated the crystalline size and the nanostructure of the CNSnS15 heterojunction synthesized by sonochemical and physical mixing processes [Fig. 5]. The g-C_3N_4 recorded a laminar sheet structure with

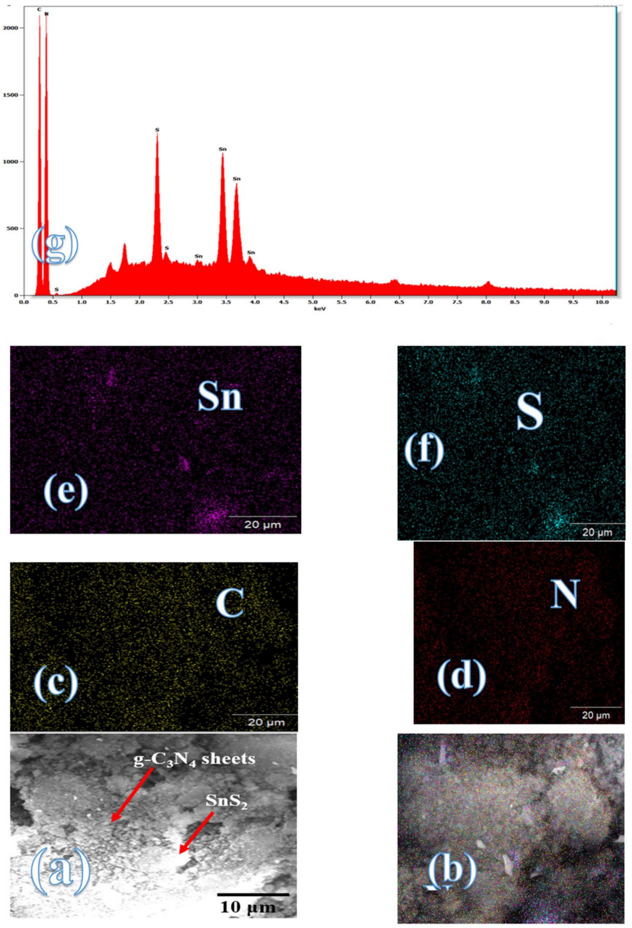

Fig. 4 (a) SEM of CNSnS15 and mapping of (b) CNSnS15, (c) C, (d) N, (e) Sn, (f) S and (g) EDX of CNSnS15 prepared using the sonochemical method.

wrinkle points and a spongy texture [Fig. 5a]. SnS_2 nanoparticles induced porous layers that prohibited the sheets with super positions for enhancing the mass diffusion reactions for pollutant molecules. Fig. 5b displays the TEM analysis of CNSnS15 synthesized by the physical mixing process that revealed the agglomeration of SnS_2 on g-C_3N_4, which hinders light penetration. The intimate contact between g-C_3N_4 sheets and SnS_2 favored the successful building of the S-scheme heterojunction for the solid sample synthesized by the sonochemical process. HRTEM recorded the interplanar distance of 0.315 and 0.267 nm, which referred to the (002) and (101) planes of g-C_3N_4 and SnS_2, respectively [Fig. 5c and d]. The SAED image of CNSnS15 [Fig. 5e and f] recorded the existence of two diffraction rings belonging to (002) and (101) planes of g-C_3N_4 and SnS_2, respectively. The experimental data extracted from Mapping, EDX, HRTEM, and SEM analyses implied the successful construction of the SnS_2/g-C_3N_4 heterojunction. XPS measurement analyzed the chemical compositions and the oxidation state of the constituents of pristine g-C_3N_4, SnS_2 and CNSnS15 nanocomposite with high precision [Fig. 6]. The C 1s spectrum in the pristine g-C_3N_4 was resolved into four deconvoluted peaks at 284.6, 285.9, 288.1 and 289.0 eV, which referred to the C–C, N–C═N and C–OH bonding, respectively [Fig. 6a]. The N 1s spectrum in the pristine g-C_3N_4 was resolved into three deconvoluted peaks at 399.1, 400.2 and 404.6 eV that ascribed to C–N═C bonding, N–$(C)_3$ bonding and CN–H bonding, respectively [Fig. 6b]. The spectrum of Sn 3d in the pristine SnS_2 nanoparticles was resolved into two peaks of Sn $3d_{3/2}$ and Sn $3d_{5/2}$ observed at 495.6 and 487.1 eV, respectively [Fig. 6c]. The S (2p) spectrum was resolved into two deconvoluted peaks at 167.8 and 169.1 eV, which ascribed to S $2p_{3/2}$ and $2p_{1/2}$ [Fig. 6d]. XPS spectrum of the CNSnS15 heterojunction showed the same characteristic peaks of C, N, Sn and S recorded in the pristine materials. The C 1s spectrum in the CNSnS15 heterojunction was resolved into four deconvoluted peaks at 284.6, 286.1, 288.3 and 289.5 eV, which referred to C–C, N–C═N and C–OH bonding, respectively [Fig. 6e]. The N 1s spectrum in the CNSnS15 heterojunction was resolved into three deconvoluted peaks at 399.1, 400.4 and 404.8 eV that ascribed to C–N═C bonding, N–$(C)_3$ bonding and CN–H bonding, respectively [Fig. 6f]. The spectrum of Sn 3d was resolved into two peaks of Sn $3d_{3/2}$ and Sn $3d_{5/2}$ observed at 495.6 and 487.3 eV [Fig. 6g]. The S (2p) spectrum was resolved into two deconvoluted peaks at 168.4 and 169.1 eV, which is ascribed to S $2p_{3/2}$ and $2p_{1/2}$ [Fig. 6h]. It is interesting to notice a little shift in the peak spectrum of C (1s), Sn (3d) and S (2p) to higher binding energy values, revealing the electron density coupling between g-C_3N_4 and SnS_2 nanoparticles, implying the successful construction of the SnS_2/g-C_3N_4 heterojunction.

Diffuse reflectance spectrum [DRS] and photoluminescence analysis [PL] investigated the optical properties of the

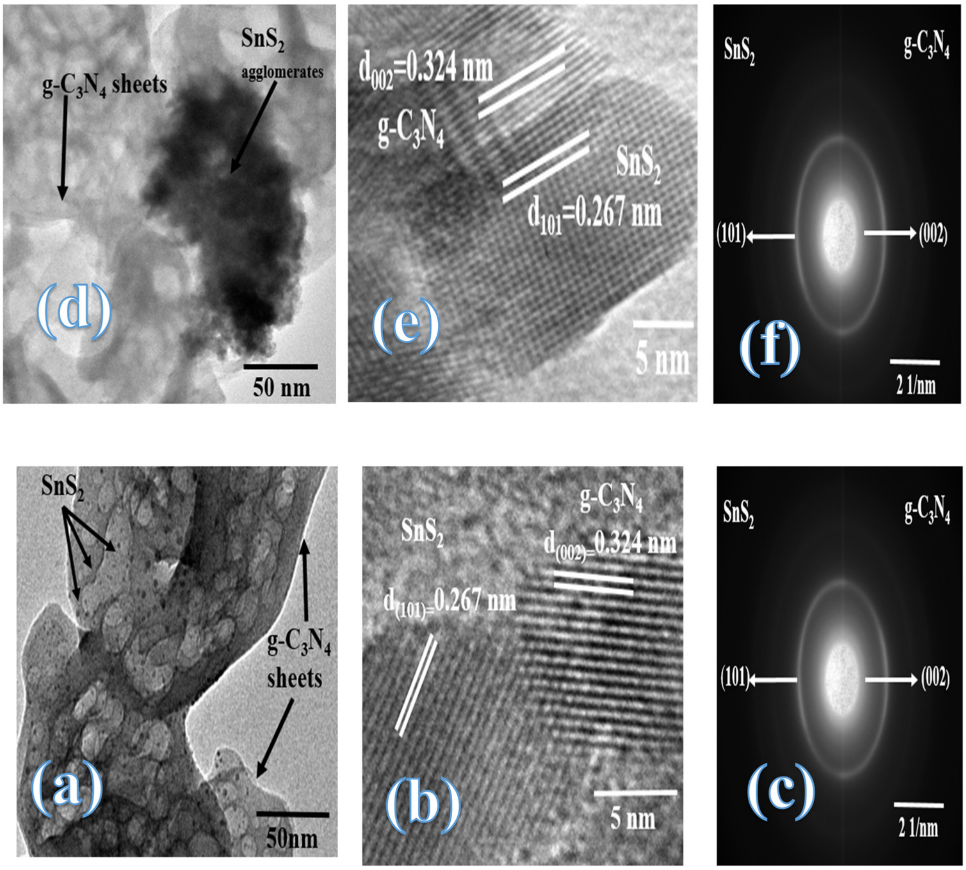

Fig. 5 (a) TEM, (b) HRTEM, (c) SAED of the CNSnS15 heterojunction prepared by employing the sonochemical process. (d) TEM, (e) HRTEM, and (f) SAED of the CNSnS15 heterojunction prepared using the physical mixing process.

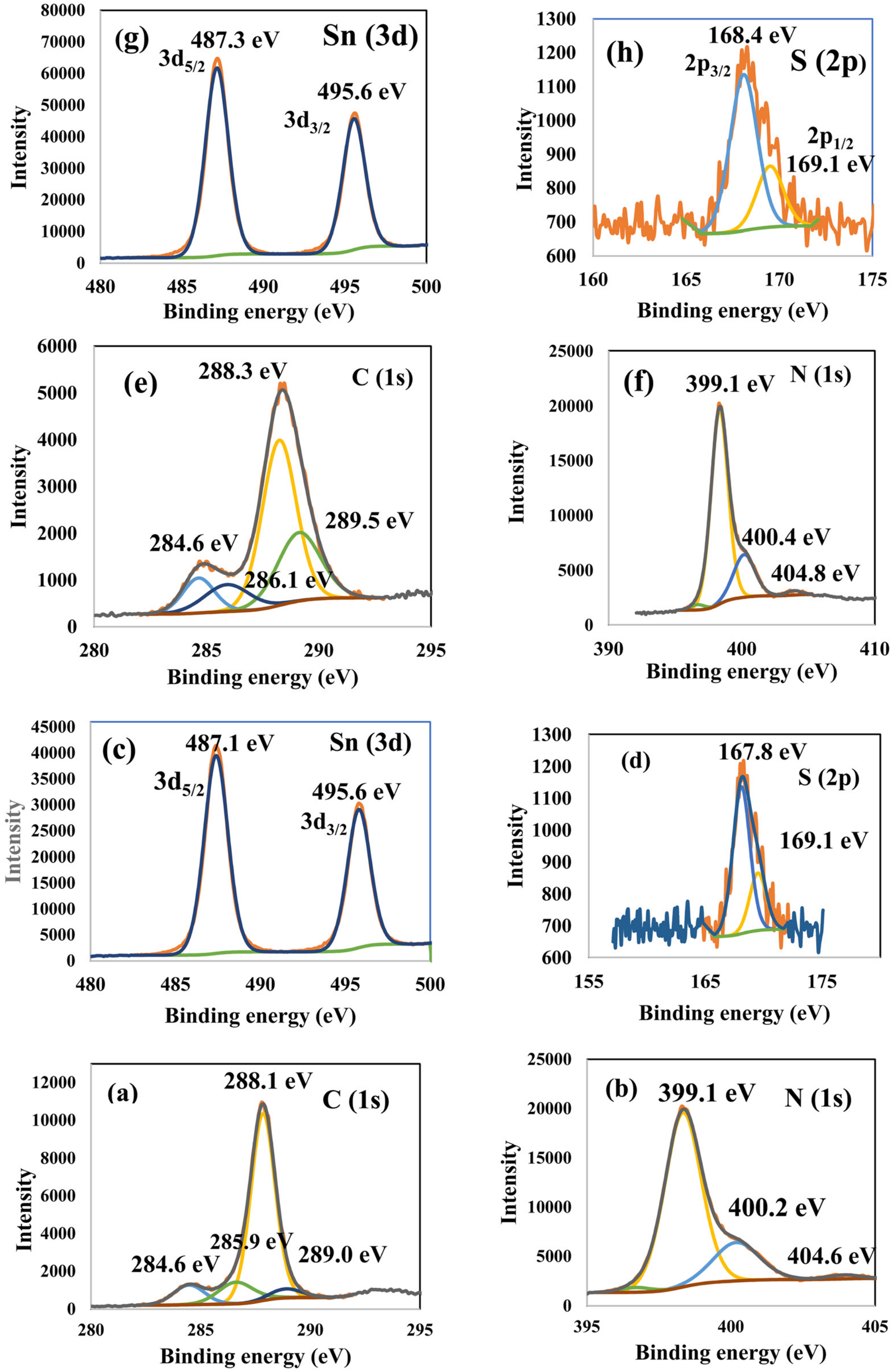

Fig. 6 XPS of (a) C and (b) N in g-C_3N_4; (c) Sn and (d) S in SnS_2; and (e) C, (f) N, and (g) Sn (h) S in CNSnS15 heterojunction prepared using the sonochemical process.

as-synthesized samples. The DRS displayed an absorption edge at 439 and 784 nm, which referred to the absorbability of g-C_3N_4 and SnS_2, respectively, implying the absorbability of g-C_3N_4 in the initial stage of the visible region; however, SnS_2 strongly absorbs the full broad spectrum of the sunlight radiation due to its narrow band gap energy [Fig. 7a]. It is interesting to notice that incorporating 15 and 20 wt% SnS_2 on the g-C_3N_4 surface enhanced the absorbability of the nanocomposite to

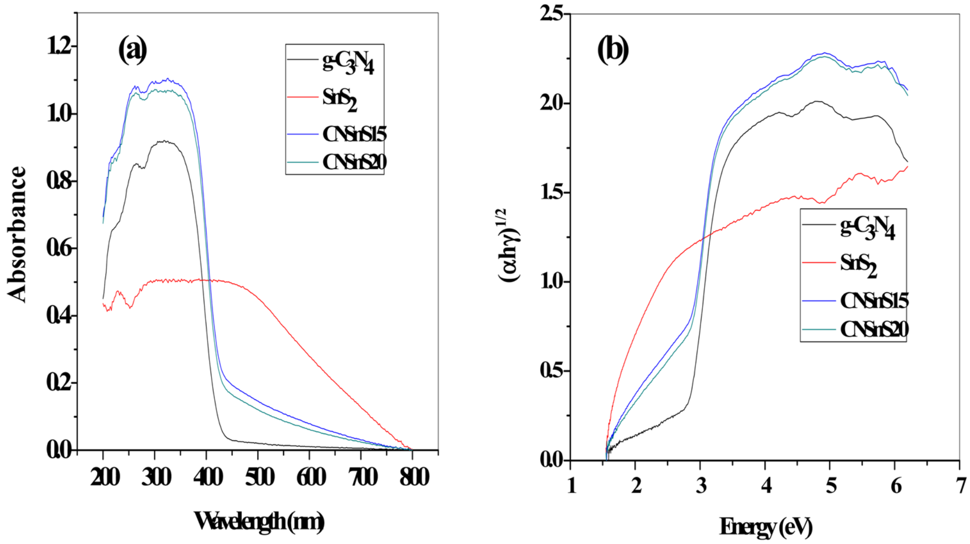

Fig. 7 (a) DRS of g-C_3N_4, SnS_2, CNSnS15 and CNSnS20 prepared through the sonochemical process, (b) Tauc plots of g-C_3N_4, SnS_2, CNSnS15 and CNSnS20 prepared through the sonochemical process.

utilize the full broad spectrum of the natural sunlight. Tauc plots represented the band gap energy from the tangent of the linear section, and the estimated band gap energy is 2.8, 1.7, 2.4 and 2.3 for g-C_3N_4, SnS_2, CNSn15 and SnS20, respectively [Fig. 7b]. The band gap energy results revealed that the electron density hybridization between g-C_3N_4 and SnS_2 decremented the band gap energy and improved the fraction of light absorbability.

The band structure, including the potential of valence and conduction band, was estimated according to the following formula to follow up the direction of electron–hole pair transport between g-C_3N_4 and SnS_2 nanoparticles:

$$E_{VB} = X_{\text{semiconductor}} - E_e + 0.5E_g \quad (1)$$

$$E_{CB} = E_{VB} - E_g \quad (2)$$

4.7 and 5.8 eV are the reported values for electronegativity [X] of g-C_3N_4 and SnS_2, respectively and E_g is the band gap energy calculated from the tangent straight line of the Tauc plot. According to the above equation, the valence and conduction band potentials are +1.6 and −1.2 V for g-C_3N_4 and +2.15 and +0.35 V for SnS_2 nanoparticles, respectively. The primary role of SnS_2 nanoparticles in improving the charge carrier separation and transportation efficiency was determined by constructing the PL spectrum of the solid specimens [Fig. 8]. The PL spectrum displayed a broad signal at 450 nm, implying the strong Coulombic electron–hole attraction force between electron–hole pairs in g-C_3N_4 sheets. Hybridizing g-C_3N_4 with 5, 10 and 15 wt% SnS_2 reduced and controlled the recombination rate of the charge carriers by 26, 30 and 40% [Fig. 8a].

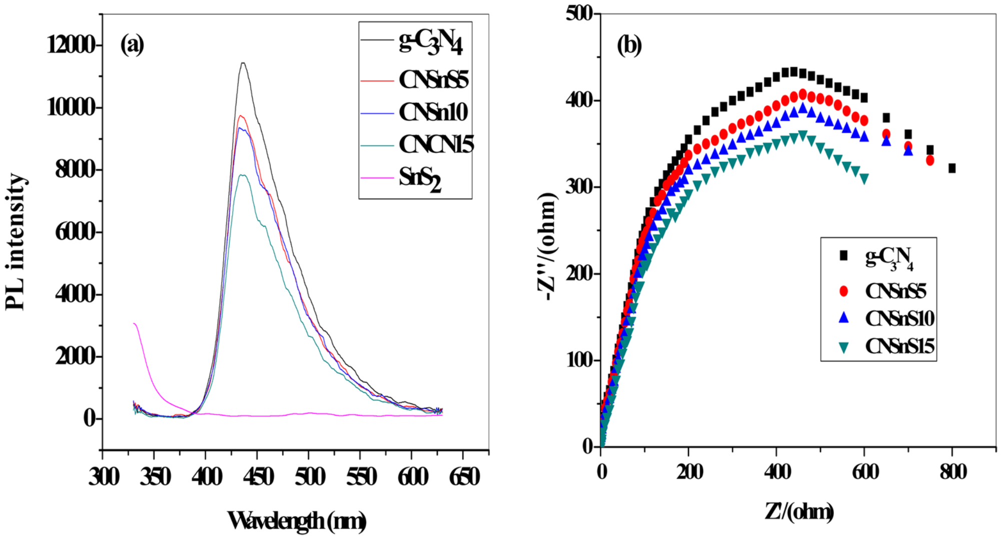

Fig. 8 (a) PL of g-C_3N_4, SnS_2, CNSnS5, CNSnS10 and CNSnS15. (b) EIS plots of g-C_3N_4, CNSnS5, CNSnS10 and CNSnS15 prepared *via* the sonochemical method.

The experimental results from PL analysis revealed that the separation and transportation efficiency of the electron–hole pairs of g-C_3N_4 was enhanced with the incorporation of various compositions of SnS_2 nanoparticles. The excitonic electron–hole pairs were generated at the conduction [CB] and valence bands [VB] due to the falling of sunlight radiations on the semiconductor surface with energy higher than the band gap energy. These generated charge carriers are responsible for redox processes at the heterojunction–solution interface. Under sunlight illumination with 1000 W power, the electrons produced and accumulated in the CB of g-C_3N_4 will diffuse to the CB of SnS_2 and then recombine with the photogenerated holes that exist in the VB of g-C_3N_4 since the VB of g-C_3N_4 is just below the CB SnS_2. However, the electron conduction band of g-C_3N_4 and positive holes of SnS_2 are preserved for a series of successful oxidation–reduction reactions for degrading organic pollutant molecules. Fig. 8b displays the electrochemical impedance spectrum [EIS] of the pristine and heterojunction samples. The Nyquist plot of the heterojunction samples has the smallest arc compared with the pristine g-C_3N_4 sheets. These experimental results implied the lowest interface resistance of electron transport in heterojunction samples, which promotes charge carrier separation. The experimental results revealed that CNSnS15 heterojunction has the lowest arc, revealing that the incorporation of 15 wt% SnS_2 improved the separation efficiency of the charge carriers, which is consistent with the results extracted from PL analysis.

3.2. The experimental photocatalytic results concerned with the degradation of RhB dye

Rhodamine B is employed in the cosmetics, food and cloth industry due to its vibrant red color and stable conjugated aromatic structure. The degradation of RhB dye was extensively investigated through traditional processes, such as coagulation, adsorption, ion exchange, reverse osmosis and microbiological methods. However, these methods are energy consumers, have high costs and may transport the primary pollutant into secondary ones, which require further treatment and analysis. Photocatalysis is an efficient low-cost process for the degradation of RhB dye molecules into non-toxic species under natural solar

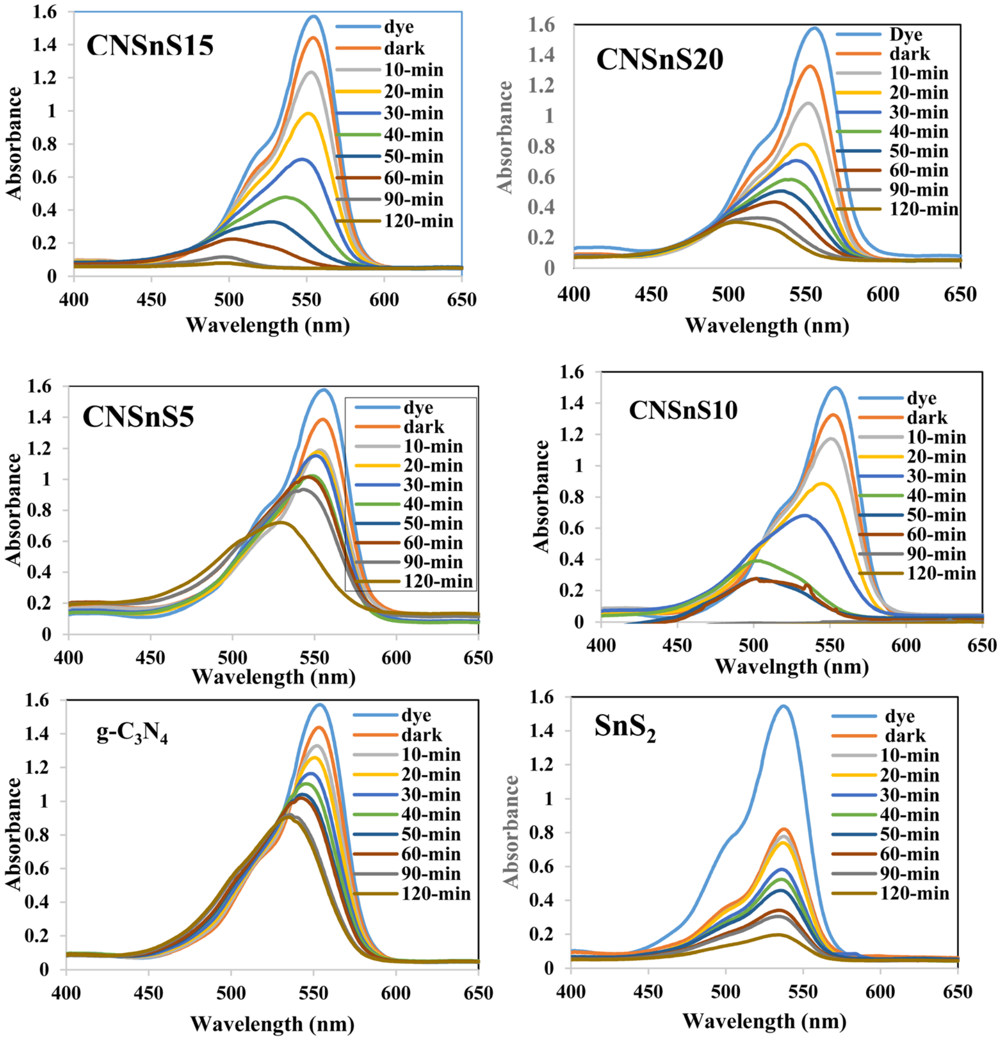

Fig. 9 Photocatalytic degradation of rhodamine B dye over the surface of the as-synthesized samples prepared using the sonochemical process.

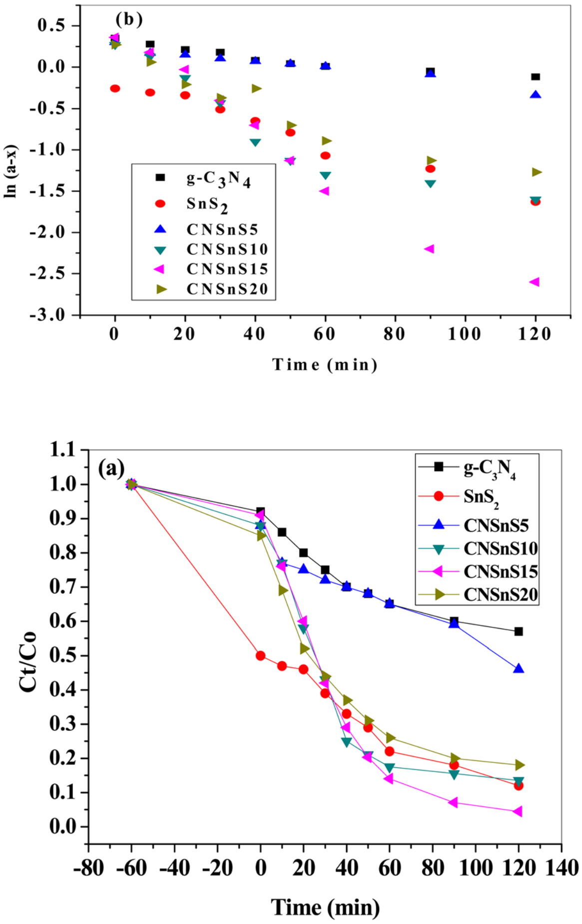

Fig. 10 (a) The variation of the photocatalytic degradation of RhB dye with time of irradiation on the surface of the as-synthesized samples. (b) Pseudo-first order plot of the photocatalytic degradation of rhodamine B dye over the surface of the as-synthesized samples.

radiation. Under sunlight illumination of 1000 W power, the photocatalytic performance of g-C_3N_4, SnS_2 and SnS_2/g-C_3N_4 heterojunctions was investigated and recorded under mild operating conditions and displayed in Fig. 9. The experimental results implied that 4% of RhB dye molecules were degraded under sunlight illumination in the absence of photocatalyst revealing the strong chemical stability of the aromatic structure of the organic dye molecules. Before exposure to natural solar radiation, the photocatalyst was mixed and stirred with the RhB dye solution for one hour to calculate the extent of the solid specimens to remove RhB dye through adsorption. The adsorption process is usually accompanied by strong deposition of dye molecules on the solid surface, which may block the active sites of the solid and hinder the recyclability of the solid specimens in various industrial applications. The experimental adsorption results revealed that the amount of RhB dye removed *via* the adsorption process did not exceed 10% over the heterojunction surface. With sunlight irradiation on the dye–solid mixture, a huge amount of radicals migrated to the semiconductor surface to mineralize RhB dye molecules. The photocatalytic profile illustrated in Fig. 9 recorded the depression in the concentration of RhB with prolonged time of solar light illumination. On examining the photocatalytic spectrum, one can notice the remarkable shift in the peak position, which is ascribed to the dissociation of RhB dye into intermediates of organic molecules. The g-C_3N_4 sheets decomposed 34% of RhB during two hours of sunlight exposure. On the contrary, SnS_2 nanoparticles degraded 78% of RhB dye by the adsorption-coupled photocatalytic process. About 50% of RhB was removed from the aqueous medium through the adsorption process on the surface of pristine SnS_2 due to the attractive force between the negatively charged surface and the cationic dye molecules. Incorporating 5 and 10 wt% of SnS_2 on g-C_3N_4 sheets enhanced the decomposition of RhB dye to 50 and 71%. Further, loading g-C_3N_4 sheets with 15 wt% SnS_2 enhanced the decomposition of RhB dye to 98%. However, a pronounced depression in the removal of RhB dye to 81% was recorded for the nanocomposite containing 20 wt% SnS_2 [Fig. 10a]. The shift in the absorption peak position of RhB dye to a lower wavelength compared with the initial dye concentration was recorded in the photocatalytic spectrum profile of RhB dye degradation on the semiconductor surface [Fig. 9]. These experimental results displayed in the spectrum of photocatalytic removal of RhB dye accounted for the generation of various chemical intermediate through a de-ethylation mechanism. In fact, the degradation of RhB proceeded through fragmentation stages that generated a series of intermediate components through the removal of ethyl groups one by one, as observed by the gradual shift in the peak position toward the lower wavelength. De-ethylation of the fully *N*,*N*,*N*-,*N*-tetra-ethylated rhodamine molecule generated *N*,*N*,*N*-tri-ethylated rhodamine at 548 nm, *N*,*N*-di-ethylated rhodamine at 539 nm, *N*-ethylated rhodamine at 518 nm and rhodamine at 499 nm. The pseudo first-order rate constant was determined from the graphical plot between the time of light illumination and $\ln(a-x)$ was 0.0039, 0.0121, 0.0047, 0.013, 0.027 and 0.017 min^{-1} for g-C_3N_4, SnS_2, CNSnS5, CNSnS10, CNSnS15 and CNSnS20 [Fig. 10b]. The precise analysis of the charge transport mechanism and type of the reactive species playing a crucial role in the photocatalytic degradation of RhB dye was investigated by scavenger trapping reagents, such as benzoquinone, isopropanol and ammonium oxalate to trap superoxide, hydroxyl radicals and positive holes, respectively. Benzoquinone, isopropanol and ammonium oxalate reduced the photocatalytic degradation of RhB dye from 98% to 53%, 34% and 82%, respectively, implying that the reactive oxygen species are the crucial species involved in the photodegradation process [Fig. 11a]. The generation of hydroxyl radicals was estimated through the hydroxylation of terephthalic acid in a basic medium under natural solar illumination. The brilliant emission peak recorded at 426 nm revealed the enhancement in the production of hydroxyl radicals $\left[E_{\mathrm{OH}^\bullet/\mathrm{H_2O}} = +1.88\,\mathrm{eV}\right]$ on the surface of the CNSnS15 heterojunction [Fig. 11b]. These results revealed that hydroxyl radicals were produced by water oxidation with positive holes of SnS_2 nanoparticles. These results were in agreement with scavenger trapping experiments that proved that hydroxyl radicals are the most effective species for dye degradation. The reusability was carried out on the optimum solid specimens under natural solar irradiation, as shown in Fig. 11c. In each cycle, the photocatalyst was washed with bi-distilled water

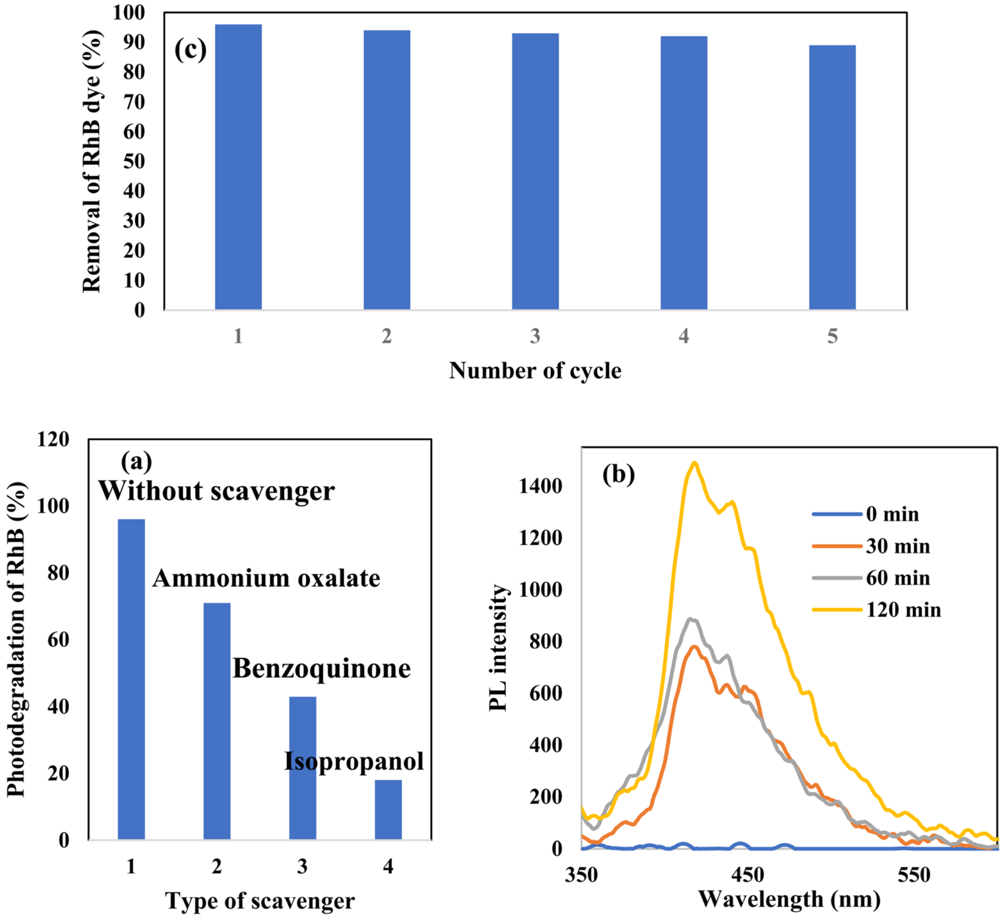

Fig. 11 (a) Effect of various scavengers on the photocatalytic degradation of RhB dye over the surface of the CNSnS15 heterojunction, (b) PL spectrum of terephthalic acid at 325 nm excitation wavelength over the CNSnS15 heterojunction and (c) recycling of CNSn15 in the photocatalytic degradation of rhodamine B for five consecutive cycles.

repeatedly before the subsequent cycle. The overall removal (%) of RhB dye did not noticeably change even after the five consecutive cycles were completed, implying the strong chemical stability of the photocatalyst in degrading the dye pollutants several times. The complete degradation of rhodamine B dye into eco-friendly species was evaluated by carrying out the total organic carbon [TOC] analysis. TOC contents fall from 71.3 mg L^{-1} to 7.5 mg mL^{-1}, accounting for the fragmentation of 90% of RhB dye, similar to the values extracted from the photocatalytic spectrum analysis.

To investigate the effect of the mode of preparation of the photocatalyst on the optical properties and the photocatalytic efficiency, the optimum sample CNSnS15 was prepared by the physical mixing process and the experimental results were compared with those recorded on the sample prepared by the sonochemical route. DRS analysis and Tauc plot represented in Fig. 12a and b revealed that the CNSnS15 photocatalyst prepared by the sonochemical route exhibited strong absorbability of visible light radiations rather than the sample synthesized by the physical mixing process. The band gap energy calculated from the Tauc plot is 2.8, 2.4 and 2.6 eV for g-C_3N_4 and CNSnS15 prepared by sonochemical and physical mixing methods, respectively. PL analysis results implied that the sample prepared by physical mixing showed a high electron–hole recombination rate, which limited the photocatalytic reactivity compared with the sample prepared by the sonochemical route [Fig. 12c]. Fig. 12d displays the electrochemical impedance spectrum [EIS] of the pristine g-C_3N_4 and CNSnS15 heterojunction prepared by sonochemical and physical mixing routes. The Nyquist plot of the CNSnS15 heterojunction has a small arc radius compared with g-C_3N_4 sheets. These experimental results implied the lowest interface resistance of electron transport in CNSnS15 heterojunctions prepared by different methods. However, CNSnS15 heterojunction prepared *via* the sonochemical route has a lower arc compared with the solid specimen prepared *via* the physical mixing method, revealing that the incorporation of 15 wt% SnS_2 under the sonochemical process enhanced the separation efficiency of charge carriers, which is consistent with the results extracted from PL analysis. The photocatalytic degradation of the RhB dye on the sample prepared by physical mixing revealed the decomposition of 55% of RhB dye compared with 96% decomposition on the sample prepared by the sonochemical route [Fig. 12e and f]. The pseudo first-order rate for the

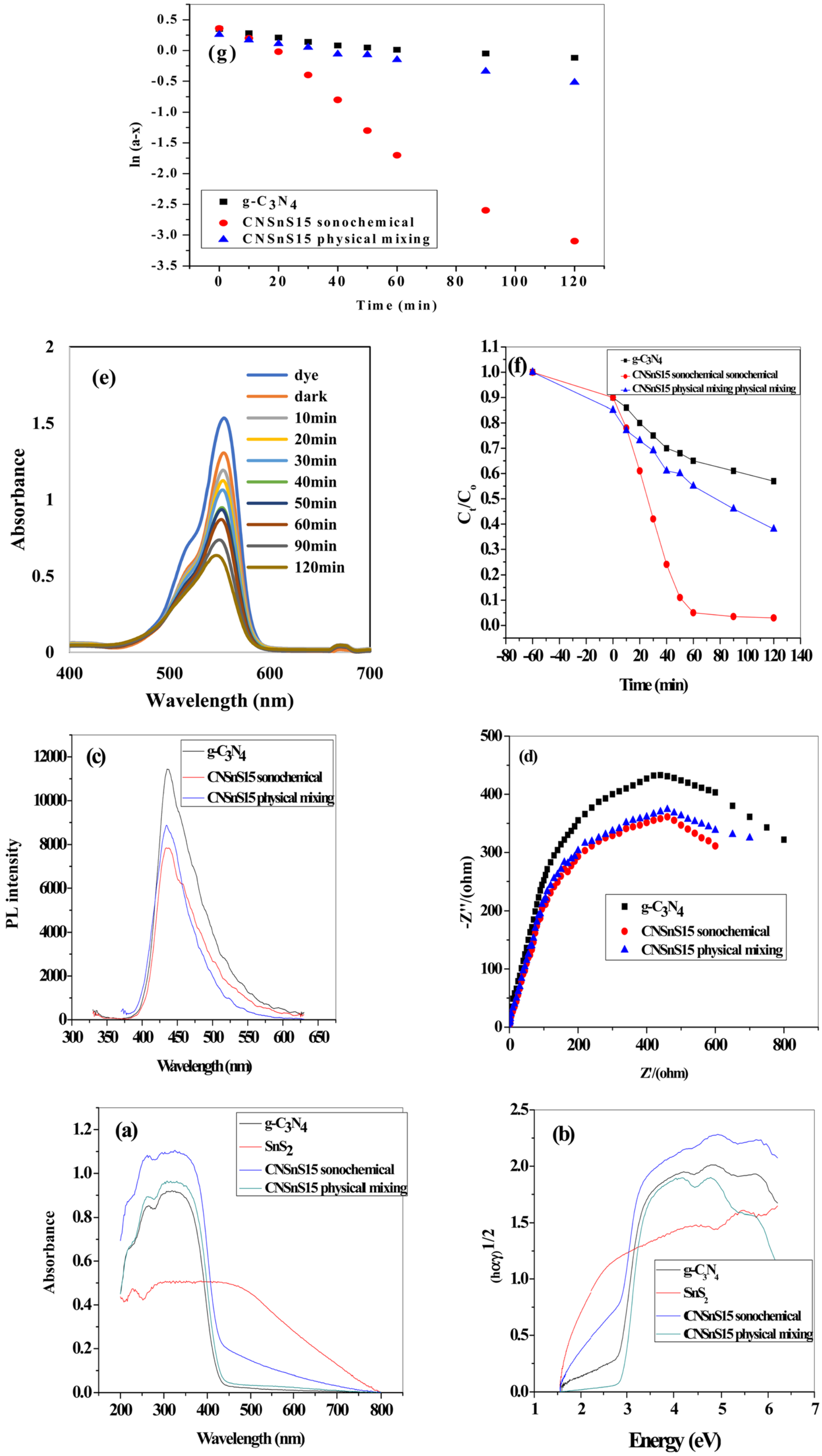

Fig. 12 (a) DRS spectrum of g-C_3N_4, CNSnS15 synthesized *via* sonochemical and physical mixing methods, (b) Tauc plot spectrum of g-C_3N_4 and CNSnS15 synthesized *via* sonochemical and physical mixing methods, (c) PL spectrum of g-C_3N_4 and CNSnS15 synthesized *via* sonochemical and physical mixing methods, (d) EIS plot of g-C3N4 and CNSnS15 prepared *via* sonochemical and physical mixing methods, (e) absorption spectrum for the photocatalytic degradation of rhodamine B dye over SnSnS15 prepared *via* the physical mixing method, (f) photocatalytic removal of RhB dye over g-C_3N_4 and CNSnS15 prepared *via* sonochemical and physical mixing methods, and (g) pseudo-first order plot for the photocatalytic removal of RhB dye over g-C_3N_4 and CNSnS15 prepared *via* sonochemical and physical mixing methods.

photocatalytic degradation of RhB dye on the surface of the sample prepared by physical mixing is 0.00165 min^{-1}, which is nearly half the rate of dye decomposition on the surface of the solid prepared by the sonochemical route [Fig. 12g]. All the above experimental results implied that the photocatalyst synthesized by the sonochemical route exhibited better electron–hole separation and transport and strong photocatalytic efficiency in degrading the RhB dye compared with the sample synthesized by the physical mixing route. The exceptional photocatalytic reactivity of the sonicated CNSnS15 was attributed to the proper dispersion of SnS_2 on g-C_3N_4 sheets as recorded in the TEM analysis, which facilitates the construction of the SnS_2/g-C_3N_4 heterojunction with remarkable high absorbability of visible light radiation and efficient electron–hole transport and separation. On the other hand, the agglomeration of SnS_2 nanoparticles on g-C_3N_4 sheets for the solid prepared by the physical mixing route reduced the light absorbability and increased the probability of the electron–hole recombination rate. These experimental results implied that the sonochemical process is an efficient route for the successful production of SnS_2/g-C_3N_4 heterojunctions with exceptional photocatalytic reactivity compared with the physical mixing process.

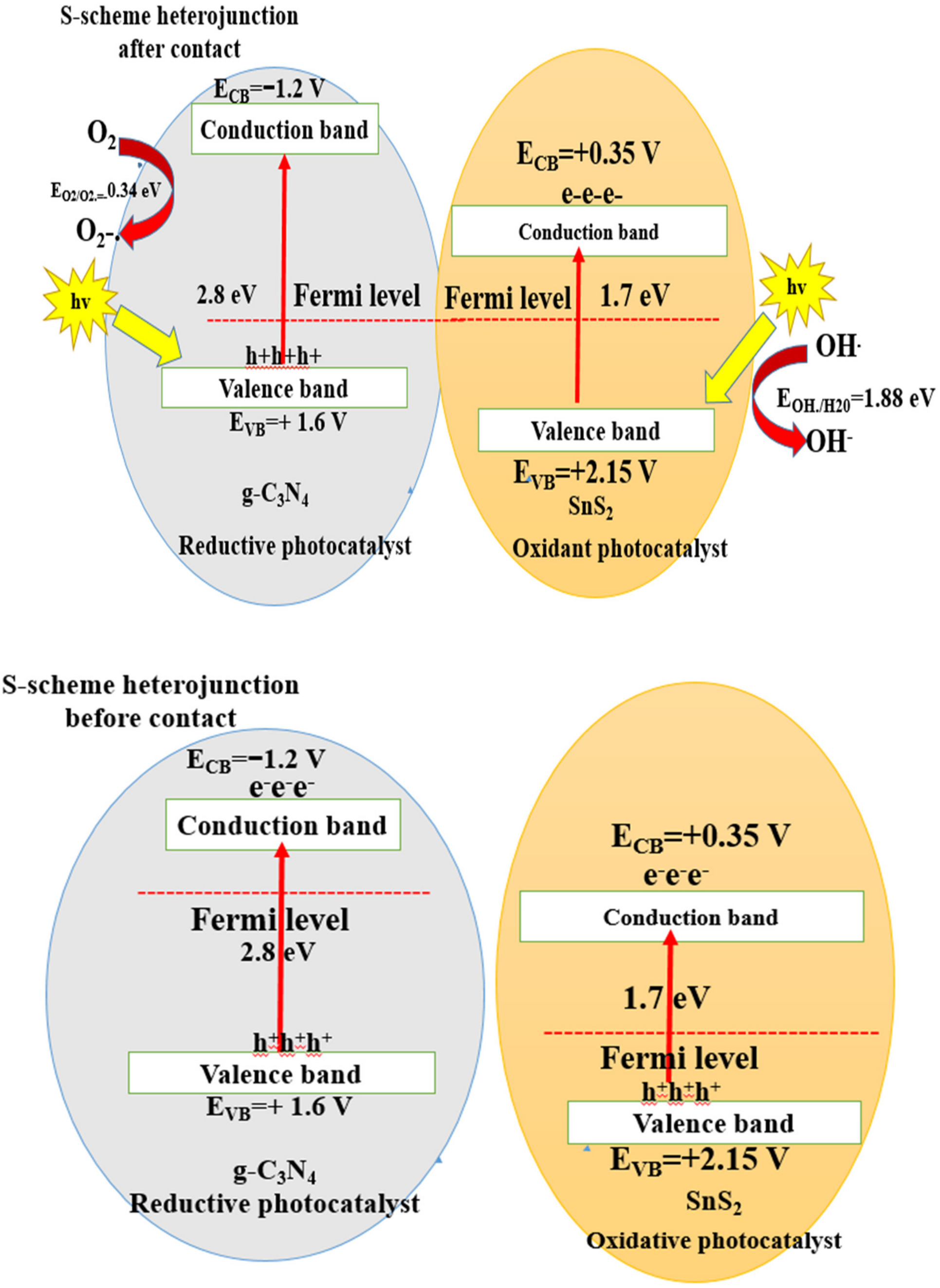

Fig. 13 S-scheme for charge transport before and after the contact of g-C_3N_4 and SnS_2 semiconductors.

Table 1 Comparative investigation of the degradation of toxic organic dyes using the SnS_2/g-C_3N_4 system

Photocatalyst	Mode of preparation	organic dye	Light source	Degradation efficiency (%)	Ref.
SnS_2/g-C_3N_4	Sonochemical	Rhodamine B	Natural sunlight	97	Our research
SnS_2/g-C_3N_4	Direct calcination	Rhodamine B	60 W–220 V lamp	95	33
SnS_2/g-C_3N_4	Ion exchange	Methyl orange	350 W xenon lamp	93	34
SnS_2/g-C_3N_4	Hydrothermal	Methyl orange	350 W visible lamp	97	35
SnS_2/g-C_3N_4	Hydrothermal	Methylene blue	300 W visible light	56	36
SnS_2/RGO/g-C_3N_4	SnS_2/g-C_3N_4	Methylene blue	300 W visible lamp	86	36
SnS_2/g-C_3N_4	Solvothermal	Rhodamine B	300 W xenon lamp	91	37
SnS_2/g-C_3N_4	Solvothermal	2,4-dichlorophenol	300 W xenon lamp	94	38
SnS_2 dot/g-C_3N_4	Solvothermal	Rhodamine B	300 W xenon lamp	96.8	39
MoS_2-SnS_2@g-C_3N_4	Hydrothermal	Methylene blue	300 W xenon lamp	86.6	40
3DF-SnS_2/g-C_3N_4	Solvothermal	Rhodamine B	400 W xenon lamp	90.15	41
SnS_2/g-C_3N_4	Calcination	Rhodamine B	60 W–220 V lamp	92.2	42
g-C_3N_4/Ag_2S/SnS_2	Sonochemical	Methyl orange	500 W xenon lamp	96.8	43
SnS_2/g-C_3N_4	Calcination	Hexavalent uranium	Sunlight	90	44

The mechanism of fragmentation of the RhB dye on the surface of the SnS_2/g-C_3N_4 heterojunction interface under sunlight illumination can be elucidated through scavenger trapping analysis and the band structure of the heterojunction. The famous type II heterojunction and the recent S-scheme mechanism can account for the diffusion of electron–hole pairs between the selected semiconductors.[46–62] Through a type-II charge transfer mode, both SnS_2 and g-C_3N_4 semiconductors absorbed a definite amount of energy and were excited to generate photoinduced negative electrons and positive holes under natural light illumination. The excited electrons in the conduction band of g C_3N_4 were simultaneously diffused to the conduction band of SnS_2 with a lower negative potential. On the contrary, the photogenerated holes were transported from the valence band of SnS_2 to that of g-C_3N_4 of a lower positive potential. Based on this charge transport, the photoinduced electrons were accumulated in the conduction band of SnS_2 with a small reduction potential, whereas photoinduced holes were accumulated on the valence band of g-C_3N_4 with a low oxidation potential. This electron transport was rejected from the thermodynamic and kinetic aspects due to the loss of charge carriers of high redox potential. Moreover, the electrons in the conduction band in SnS_2 fail to generate the superoxide radicals $\left(E_{O_2/O_2^{\bullet-}} = -0.34\,\text{eV}\right)$ and the positive holes in the valence band of g-C_3N_4 fail to oxidize water and generate hydroxyl radicals $\left(E_{H_2O/OH^{\bullet}} = +1.88\,\text{eV}\right)$. The experimental results of the PL spectrum of terephthalic acid and the scavenger trapping experiments implied the production of hydroxyl and superoxide radicals, which reject the aspects of charge transport through the type (II) mechanism. The S-scheme charge migration is a more precise mechanism in elucidating the proper direction of the electron–hole diffusion route [Fig. 13]. On direct irradiation of sunlight on the heterojunction interface, electrons were diffused from g-C_3N_4 to SnS_2, generating the depletion and accumulation layers at the interface boundary of g-C_3N_4 and SnS_2, respectively. This electron migration marked a negative and positive charge on SnS_2 and g-C_3N_4 regions, respectively. Due to simultaneous charge diffusion, an internal electric field traversed from the g-C_3N_4 to the SnS_2 side. The Fermi levels of g-C_3N_4 and SnS_2 move upwards and downwards to reach an equalization position at the interface region between SnS_2 and g-C_3N_4 sheets. At this neutralized region, the weak charge carriers of g-C_3N_4 (E_{VB} = +1.6 V) and SnS_2 (E_{CB} = +0.1 V) are removed by the electrostatic attraction force. However, the positive hole of SnS_2 (E_{VB} = +2.28 eV) and electrons of g-C_3N_4 (E_{CB} = −1.2 V) were maintained for playing a crucial role in the redox process. The photocatalytic experimental results of SnS_2/g-C_3N_4 in this research were compared with the recent studies [Table 1]. The results recorded in Table 1 revealed that the sonicated SnS_2/C_3N_4 synthesized by the sonochemical route displayed an excellent photocatalytic performance in the removal of various organic pollutants compared with the nanocomposites synthesized by the hydrothermal, solvothermal and ion exchange processes.[33–42] Moreover, various recent research studies revealed that the addition of RGO,[36] MoS_2[40] and Ag_2S[43] was required to facilitate the charge diffusion between SnS_2 and g-C_3N_4. All the previous photocatalytic processes on the mineralization of organic pollutants under UV and visible light sources are expensive and exhibit limited power to employ on an industrial scale. However, the degradation of RhB dye as a cationic pollutant model was carried out in our research under natural sunlight radiation, considering the low cost and the available illumination source in our country.

Conclusions

Herein, the adjusted S-scheme SnS_2/g-C_3N_4 heterojunction with an aligned band structure and a narrow mesoporous texture were synthesized by sonochemical and physical mixing processes for solar degradation of rhodamine B dye under natural sunlight radiation of 1000 W power. SnS_2 nanoparticles with 1.7 eV band gap energy were dispersed sonochemically on the wrapped g-C_3N_4 sheets in localized positions, generating a porous sheet structure that facilitates the transport of organic dye molecules. However, the agglomeration of SnS_2 nanoparticles on g-C_3N_4 sheets was recorded for the heterojunction synthesized by the physical mixing process, which restricts the light transport to the photocatalyst surface and reduces the photocatalytic efficiency. DRS, PL, HRTEM, N_2-adsorption–desorption isotherms, SEM, EIS and SAED analyses verified the engineering of the SnS_2/g-C_3N_4 heterojunction with excellent absorbability of sunlight radiation and better transport and separation of electron–hole pairs. PL analysis of an alkaline solution of terephthalic acid detected the solar production of hydroxyl radicals. However, the experimental trapping agents elucidated the direction of the charge carrier transport by adopting the concept of the S-scheme heterojunction. Thoroughly, in the S-scheme process, the undesirable holes and electrons of g-C_3N_4 and SnS_2 with weak redox potentials were removed by the electrostatic attraction force at the interface boundary of the semiconductors surface. On the contrary, SnS_2 positive holes and g-C_3N_4 electrons degraded RhB dye molecules under sunlight illumination. The photocatalytic optimized experiments recorded that the sonicated nanocomposite CNSnS15 with 15 wt% SnS_2 degraded 96% of RhB dye and exhibited strong stability in the mineralization of the toxic organic dye for five consecutive cycles. The novel SnS_2/g-C_3N_4 heterojunction with extra-ordinary redox efficiency under natural sunlight radiation is considered a promising photocatalyst for the degradation of various toxic organic pollutants.

Data availability

Data will be made available on request.

Conflicts of interest

There are no conflicts to declare.

Acknowledgements

We are grateful for the financial support by the Researchers Supporting Project number (RSP2024R78), King Saud University, Riyadh, Saudi Arabia

References

1. M. Adel, M. A. Ahmed and A. A. Mohamed, Effective removal of cationic dyes from aqueous solution using reduced graphene oxide functionalized with manganese ferrite nanoparticles, *Compos. Commun.*, 2020, **22**, 100450.
2. M. Adel, M. A. Ahmed, M. Adel, M. A. Ahmed and A. A. Mohamed, Synthesis and characterization of magnetically separable and recyclable crumbled $MgFe_2O_4$/reduced graphene oxide nanoparticles for removal of methylene blue dye from aqueous solutions, *J. Phys. Chem. Solid*, 2021, **149**, 109760.
3. M. A. Ahmed and Z. M. Abou-Gamra, Mesoporous MgO nanoparticles as a potential sorbent for removal of fast orange and bromophenol dyes, *Nanotechnol. Environ. Eng.*, 2016, **1**(10), 2–11.
4. M. Adel, M. A. Ahmed and A. A. Mohamed, A facile and rapid removal of cationic dyes using hierarchically porous reduced graphene oxide decorated with manganese ferrite, *Flat Chem*, 2021, **26**, 100233.
5. M. A. Ahmed, Z. M. Abou-Gamra, M. A. ALshakhanbeh and H. Medien, Control synthesis of metallic gold nanoparticles homogeneously distributed on hexagonal ZnO nanoparticles for photocatalytic degradation of methylene blue dye, *Environ. Nanotechnol. Monitor. Manag.*, 2019, **12**, 100217.
6. M. A. Ahmed, A. Fahmy, M. G. Abo-Zaed and E. M. Hashem, Fabrication of novel $AgIO_4$/SnO_2 heterojunction for photocatalytic hydrogen production through direct Z-scheme mechanism, *J. Photochem. Photobiol.*, 2020, **400**, 112660.
7. A. Alsulmi, N. N. Mohammed, M. M. Hassan, M. A. Eltawil, A. E. Amin, M. Fahmy and M. A. Ahmed, Rational engineering of S-scheme CeO_2/g-C_3N_4 heterojunctions for effective photocatalytic destruction of rhodamine B dye under natural solar radiations, *Colloids Surf., A*, 2024, **689**, 133683.
8. A. Al Fawaz, A. Alsalme, A. Soltan, M. G. Elmahgary and M. A. Ahmed, Polyaniline/g-C_3N_4 hybrid nanoparticles: Fabrication, characterization and boosting bisphenol destruction and hydrogen gas evolution through direct S-scheme aspects, *J. Phys. Chem. Solid*, 2022, **168**, 110773.
9. M. Beneissa, N. Abbas, S. Al Arni, N. Elboughdiri, A. Moumen, M. S. Hamdy, H. S. M. Abd-Rabboh, A. H. Galal, M. Gad Al-Metwaly and M. A. Ahmed, $BiVO_3$/g-C_3N_4 S-scheme heterojunction nanocomposite photocatalyst for hydrogen production and RhB dye removal, *Opt. Mater.*, 2021, **118**, 111237.
10. H. S. M. Abd-Rabboh, A. H. Galal, R. A. Aziz and M. A. Ahmed, novel $BiVO_3$/SnO_2 step S-scheme nano heterojunction for an enhanced visible light photocatalytic degradation of RhB dye and hydrogen production, *R. Soc. Chem. Adv.*, 2021, **11**, 29507.
11. Q. Xu, L. Zhang, B. Cheng, J. Fan and J. Yu, S-Scheme Heterojunction Photocatalyst, *Chem*, 2020, **6**, 1543–1559.
12. E.-H. Hashem, A. Fahmy, A. Abbas, M. Tarek, B. Mahran and M. A. Ahmed, Fabrication of novel $AgIO_4$/TiO_2 heterojunction for photocatalytic hydrogen production through direct Z-scheme mechanism, *Nanotechnol. Environ. Eng.*, 2020, **5**, 17.
13. Y. Zhang, G. M. Wang, B. Ma and Z. Jin, CdS pen heterojunction co-boosting with Co_3O_4 and Ni-MOF-74 for photocatalytic hydrogen evolution, *Dalton Trans.*, 2018, **47**, 1176.
14. A. Alsalme, A. H. Galal, E. F. El-Sherbeny, A. Soltan, M. F. Abdel-Messih and M. A. Ahmed, Fabrication of S-scheme TiO_2/g-C_3N_4 nanocomposites for generation hydrogen gas and removal of fluorescein dye, *Diam. Relat. Mater.*, 2022, **122**, 108819.
15. L. Jing, D. Wang, Y. Xu, M. Xie, J. Yan, M. He, Z. Song, H. Xu and H. Li, Porous defective carbon nitride obtained by a universal method for photocatalytic hydrogen production from water splitting, *J. Colloid Int. Sci.*, 2020, **566**, 171–182.
16. W. Niu, K. Marcus, L. Zhou, Z. Li, L. Shi, K. Liang and Y. Yang, Enhancing electron transfer and electrocatalytic activity on crystalline carbon-conjugated g-C_3N_4, *ACS Catal.*, 2018, **8**, 1926–1931.
17. M. A. E. Wafi, M. A. Ahmed, H. S. Abdel-Samad and H. A. A. Medien, Exceptional removal of methylene blue and p-aminophenol dye over novel TiO_2/RGO nanocomposites

by tandem adsorption-photocatalytic processes, *Mater. Sci. Energy Technol.*, 2022, **5**, 217–231.

18 H. S. M. Abd-Rabboh, A. H. Galal, A. M. Basely, F. M. Helmy and M. A. Ahmed, Boosting hydrogen gas production and mitigation of fluorescein dye on the surface of S-scheme g-C_3N_4/SnO_2 heterojunction, *Desalin. Water Treatment*, 2022, **268**, 113–125.

19 M. S. Hamdy, H. S. M. Abd-Rabboh, M. Beneissa, M. G. Al-Metwaly, A. H. Glal and M. A. Ahmed, Fabrication of novel polyaniline/ZnO heterojunction for exceptional photocatalytic hydrogen production and degradation of fluorescein dye through direct Z-scheme mechanism, *Opt. Mater.*, 2021, **117**, 111198.

20 A. Alsalme, M. M. Hassan, M. A. Eltawil, A. E. Amin, A. Soltan, M. F. Abdel Messih and M. A. Ahmed, Rational sonochemical engineering of Ag_2CrO_4/g-C_3N_4 heterojunction for eradicating RhB dye under full broad spectrum, *Heliyon*, 2024, **10**, 3122.

21 H. Yu, L. Shang, T. Bian, R. Shi, G. I. N. Waterhouse, Y. Zhao, C. Zhou, L. Z. Wu, C. H. Tung and T. Zhang, Carbon nanosheets: nitrogen-doped porous carbon nanosheets templated from g-C_3N_4 as metal-free electrocatalysts for efficient oxygen reduction reaction, *Adv. Mater.*, 2016, **28**, 5140.

22 S. Tian, Z. Wang, W. Gong, W. Chen, Q. Feng, Q. Xu, C. Chen, C. Chen, Q. Peng, L. Gu, H. Zhao, P. Hu, D. Wang and Y. Li, Temperature-controlled selectivity of hydrogenation and hydrodeoxygenation in the conversion of biomass molecule by the Ru1/mpg-C_3N_4 catalyst, *J. Am. Chem. Soc.*, 2018, **140**, 11161–11164.

23 H. Liu, X. Liu, W. Yang, M. Shen, S. Geng, C. Yu, B. Shen and Y. Yu, Photocatalytic dehydrogenation of formic acid promoted by a superior PdAg@g-C_3N_4 Mott Schottky heterojunction, *J. Mater. Chem. A*, 2019, **7**, 2022–2026.

24 C. Li, Y. Du, D. Wang, S. Yin, W. Tu, Z. Chen, M. Kraft, G. Chen and R. Xu, Unique P-CoN surface bonding states constructed on g-C_3N_4 nanosheets for drastically enhanced photocatalytic activity of H_2 evolution, *Adv. Funct. Mater.*, 2017, 1604328.

25 C. Li, Y. Xu, W. Tu, G. Chen and R. Xu, Metal-free photocatalysts for various applications in energy conversion and environmental purification, *Green Chem.*, 2017, **19**, 882–899.

26 M. Mousavi, A. Habibi-Yangjeh and S. R. Pouran, Review on magnetically separable graphitic carbon nitride-based nanocomposites as promising visible-light-driven photocatalysts, *J. Mater. Sci: Mater. Electron.*, 2018, **29**, 1719–1747.

27 N. Al-Zaqri, A. Alsalme, M. A. Ahmed and A. H. Galal, Construction of novel direct Z-scheme AgIO4-g-C3N4 heterojunction for photocatalytic hydrogen production and photodegradation of fluorescein dye, *Diam. Relat. Mater.*, 2020, **109**, 108071.

28 M. Mousavi, A. Habibi-Yangjeh and S. R. Pouran, Review on magnetically separable graphitic carbon nitride-based nanocomposites as promising visible-light-driven photocatalysts, *J. Mater. Sci.: Mater. Electron.*, 2018, **29**, 1719–1747.

29 I. Fareed, M. H. Farooq, M. D. Khan, M. Tahir and F. K. Butt, An efficient multifunctional SnS_2/g-C_3N_4 hierarchical nanoflower catalyst for electrocatalytic and photocatalytic applications, *Ceram. Int.*, 2024, **50**, 36004–36017.

30 Y. Mao, H. Yin, B. Qiu, J. Yao, M. Zhang, X. Liu and S. Chen, In-suit synthesis of a novel Z-scheme SnS_2/$Zn_{0.78}Cd_{0.22}S$ heterostructure with excellent photocatalytic performance, *J. Alloys Compd.*, 2021, **856**, 157423.

31 T. Qiang, L. Chen, Y. Xia and X. Qin, Dual modified MoS_2/SnS_2 photocatalyst with Z-scheme heterojunction and vacancies defects to achieve a superior performance in Cr (VI) reduction and dyes degradation, *J. Clean. Prod.*, 2021, **291**, 125213.

32 J. Chen, Z. Hong, Y. Chen, B. Lin and B. Gao, One-step synthesis of sulfur-doped and nitrogen-deficient g-C_3N_4 photocatalyst for enhanced hydrogen evolution under visible light, *Mater. Lett.*, 2015, **145**, 129–132.

33 T. H. N. Thi, H. T. Huu, H. N. Phi, V. P. Nguyen, Q. D. Le, L. N. Thi, T. T. T. Phan and V. Vo, A facile synthesis of SnS_2/g-C_3N_4 S-scheme heterojunction photocatalyst with enhanced photocatalytic performance, *J. Sci.: Adv. Mater. Devices*, 2022, **7**, 100402.

34 Y. Liu, P. Chen, Y. Chen, H. Lu, J. Wang, Z. Yang, Z. Lu, M. Li and L. Fang, In situ ion-exchange synthesis of SnS_2/g-C_3N_4 nanosheets heterojunction for enhancing photocatalytic activity, *RSC Adv.*, 2016, **6**, 10802.

35 D. Gao, D. Jiao, F. Chen, Y. Liang, Y. Wang, G. He, W. Li and Q. He, Improved photocatalytic performance of Z-scheme heterostructured SnS_2/Sg-C_3N_4 composite: A new route to increasing specific surface area, *Vacuum*, 2023, **210**, 111785.

36 S. C. Shyagathur, A. H. N. Rao, P. K. Ravishankar, G. Nagaraju and J. Pattar, SnS_2 based SnS_2/rGO/g-C_3N_4 Z-scheme ternary nanocomposites for efficient visible light-driven photocatalytic activity, *Opt. Mater.*, 2024, **147**, 114688.

37 Y. Cheng, J. He and P. Yang, Construction of layered SnS_2 and g-C_3N_4 nanoaechitectonics towards pollution degradation and H_2 generation, *Colloids Surf., A*, 2024, **680**, 132678.

38 T. Song, X. Zhang, Q. Che and P. Yang, Heterojunction nanoarchitectonics with SnS_2/g-C_3N_4 S-scheme toward enhanced photooxidation and photoreduction, *J. Ind. Eng. Chem.*, 2022, **113**, 389–400.

39 A. Zhu, L. Qiao, Z. Jia, P. Tan, Y. Liu, Y. Ma and J. Pan, C–S bond induced ultrafine SnS_2 dot/porous g-C_3N_4 sheet 0D/2D heterojunction: synthesis and photocatalytic mechanism investigation, *Dalton Trans.*, 2017, **46**(48), 17032–17040.

40 K. Tamilarasu, R. Ranjith, A. Priyadharsan, T. Rojviroon, P. Maadeswaran and S. Suganya, S., C. Umarani, Hierarchical MoS_2–SnS_2@ g–C_3N_4 Nanocomposite as an Efficient and Sustainable Material for Environmental Remediation, *J. Cluster Sci.*, 2024, **35**(2), 561–573.

41 K. M. Alnahdi, Boosted visible-light photocatalysis via p-n heterojunction synergy in 3D tin Sulfide-Graphitic carbon nitride nanohybrids, *Inorg. Chem. Commun.*, 2024, **160**, 111870.

42 T. Thi, H. N. Huu, H. N. Phi, V. P. Nguyen, Q. D. Le, L. N. Thi and V. Vo, A facile synthesis of SnS_2/g-C_3N_4 S-scheme heterojunction photocatalyst with enhanced photocatalytic performance, *J. Sci. Adv. Mater. Dev.*, 2022, **7**(2), 100402.

43 Z. Fan, J. Luan, C. Zhu and F. Liu, Depositing Ag_2S quantum dots as electron mediators in $SnS_2/g\text{-}C_3N_4$ nanosheet composites for constructing Z-scheme heterojunction with enhanced photocatalytic performance, *Mater. Res. Bull.*, 2021, **133**, 111045.

44 C. Liu, Z. Dong, C. Yu, J. Gong, Y. Wang, Z. Zhang and Y. Liu, Study on photocatalytic performance of hexagonal SnS2/g-C3N4 nanosheets and its application to reduce U (VI) in sunlight, *Appl. Surf. Sci.*, 2021, **537**, 147754.

45 P. Adamou, S. M. Al-Salem, E. Harkou, A. Constantinou, S. Hafeez, G. Manos and N. Dimitratos, Recent progress on sonochemical production for the synthesis of efficient photocatalysts and the impact of reactor design, *Ultrason. Sonochem.*, 2023, **100**, 106610.

46 S. Wageh, A. A. Al-Ghamdi and R. J. X. Li, Peng Zhang, A new heterojunction in photocatalysis: S-scheme heterojunction, *Chinese J. Catal.*, 2021, **42**, 667–669.

47 A. Alsulmi, N. N. Mohammed, A. Soltan, M. F. Abdel Messih and M. A. Ahmed, Engineering S-scheme CuO/ZnO heterojunctions sonochemically for eradicating RhB dye from wastewater under solar radiation, *RSC Adv.*, 2023, **13**, 13269.

48 A. Meng, B. Cheng, H. Tan, J. Fan, C. Su and J. Yu, TiO_2/polydopamine S-scheme heterojunction photocatalyst with enhanced CO_2-reduction selectivity, *Appl. Catal. Environ.*, 2021, **289**, 120039.

49 A. Alsulmi, M. H. Shaker, A. M. Basely, M. F. Abdel-Messih, A. Sultan and M. A. Ahmed, Engineering S-scheme $Ag_2CO_3/g\text{-}C_3N_4$ heterojunctions sonochemically to eradicate Rhodamine B dye under solar irradiation, *RSC Adv.*, 2023, **13**, 12229.

50 Q. Li, W. Zhao, Z. Zhai, K. Ren, T. Wang, H. Guan and H. Shi, 2D/2D $Bi_2MoO_6/g\text{-}C_3N_4$ S-scheme heterojunction photocatalyst with enhanced visible-light activity by Au loading, *J. Mater. Sci. Technol.*, 2020, **56**, 216–226.

51 S. Jiang, J. Cao, M. Guo, D. Cao, X. Jia and H. Lin, Shifu Chen, Novel S-scheme WO_3/RP composite with outstanding overall water splitting activity for H_2 and O_2 evolution under visible light, *Appl. Surf. Sci.*, 2021, **558**, 149882.

52 X. Zhang, Y. Zhang, X. Jia, N. Zhang, R. Xia, X. Zhang, Z. Wang and M. Yu, In situ fabrication of a novel S-scheme heterojunction photocatalyts $Bi_2O_3/P\text{-}C_3N_4$ to enhance levofloxacin removal from water, *Sep. Purif. Technol.*, 2021, **268**, 118691.

53 K. Zhang, D. Li, Q. Tian, H. Cao, F. Orudzhev, I. A. Zvereva, J. Xu and C. Wang, Recyclable 0D/2D $ZnFe_2O_4/Bi_5FeTi_3O_{15}$ S-scheme heterojunction with bismuth decoration for enhanced visible-light-driven tetracycline photodegradation, *Ceram. Int.*, 2021, **47**, 17109–17119.

54 S. Wu, X. Yu, J. Zhang, Y. Zhang, Y. Zhu and M. Zhu, Construction of $BiOCl/CuBi_2O_4$ S-scheme heterojunction with oxygen vacancy for enhanced photocatalytic diclofenac degradation and nitric oxide removal, *Chem. Eng. J.*, 2021, **411**, 128555.

55 V. V. Pham, D. Q. Mai, D. P. Bui, T. V. Man, B. Zhu, L. Zhang, J. Sangkaworn, J. Tantirungrotechai, V. Reutrakul and T. M. Cao, Emerging 2D/0D $g\text{-}C_3N_4/SnO_2$ S-scheme photocatalyst: New generation architectural structure of heterojunctions toward visible-light-driven NO degradation, *Environ. Pollut.*, 2021, **286**, 117510.

56 X. Liu, S. Wang, J. Cao, J. Yu, J. Dong, Y. Zhao, F. Zhao, D. Zhang and X. Pu, Anchoring $ZnIn_2S_4$ nanosheets on cross-like $FeSe_2$ to construct photothermal-enhanced S-scheme heterojunction for photocatalytic H2 evolution, *J. Colloid Interface Sci.*, 2024, **673**, 463–474.

57 D. Zhang, D. Zhang, S. Wang, H. Li, J. Liu, X. Pu, P. Chen, R. Qin, H. Hu and P. Cai, Synthesize magnetic $ZnFe_2O_4$@C/$Cd_{0.9}Zn_{0.1}S$ catalysts with S-scheme heterojunction to achieve extraordinary hydrogen production efficiency, *J. Colloid Interface Sci.*, 2024, **657**, 672–683.

58 P. Su, D. Zhang, M. Zhu, T. Liang, N. Yang, H. Zhao, D. Zhang, J. Liu, P. Cai and X. Pu, Re-usable Cd0.9Zn0.1S-ZnO@C/PVDF piezo-photocatalytic film with exceptional hydrogen evolution capability triggered by the synergetic advantages of piezoelectricity and S-Scheme heterojunction, *J. Energy Chem.*, 2024, **96**, 164–176.

59 J. Yu, J. Dong, X. Su, J. Yang, D. Zhang, J. Liu, P. Cai and Z. Li, D/Zhang, X. Pu, Preparation and characterization of $AgVO_3/Ag_4V_2O_7$/BiOI double S-scheme heterojunctions for the photocatalytic degradation of methylene orange and tetracycline, *J. Alloys Compd.*, 2024, **987**, 174187.

60 S. Yuan, X. Liang, Y. Zheng, Y. Chu, X. Ren, Z. Zeng, G. Nan, Y. Wu and Y. He, Enhanced piezocatalytic and piezo-photocatalytic dye degradation via S-scheme mechanism with photodeposited nickel oxide nanoparticles on $PbBiO_2Br$ nanosheets, *J. Colloid Interface Sci.*, 2024, **670**, 373–384.

61 C. Zhao, X. Li, L. Yue, S. Yuan, X. Ren, Z. Zeng, X. Hu, Y. Wu and Y. He, One-step preparation of novel $Bi\text{-}Bi_2O_3/CdWO_4$ Z-scheme heterojunctions with enhanced performance in photocatalytic NH3 synthesis, *J. Alloys Compd.*, 2023, **968**, 171956.

62 S. Yuan, J. Wang, C. Zhao, L. Yue, X. Ren, Z. Zeng, X. Hu, Y. Wu and Y. He, S-scheme Bi2O3/CdMoO4 hybrid with highly efficient charge separation for photocatalytic N2 fixation and tetracycline Degradation: Fabrication, catalytic Optimization, physicochemical studies, *Sep. Purif. Technol.*, 2023, **325**, 124665.